

A Thesis

entitled

Smart Piezoelectric Calcium Phosphates for Orthopedic, Spinal-fusion and Dental

Applications

by

Naresh Koju

Submitted to the Graduate Faculty as partial fulfillment of the requirements for the

Master of Science Degree in

Mechanical Engineering

Dr. Sarit B. Bhaduri, Committee Chair

Dr. Mehdi Pourazady, Committee Member

Dr. Matthew Franchetti, Committee Member

Dr. Amanda Bryant-Friedrich, Dean
College of Graduate Studies

The University of Toledo

May 2018

Copyright 2018, Naresh Koju

This document is copyrighted material. Under copyright law, no parts of this document may be reproduced without the expressed permission of the author.

An Abstract of

Smart Piezoelectric Calcium Phosphates for Orthopedic, Spinal-fusion and Dental Applications

by

Naresh Koju

Submitted to the Graduate Faculty as partial fulfillment of the requirements for the Master of Science Degree in Mechanical Engineering

The University of Toledo
May 2018

Calcium phosphate (CaP) compounds have been used as orthopedic, spinal and dental implants, and bone graft substitutes for several decades. Their good biocompatibility and bioactivity and most importantly their resemblance to bone and teeth mineral, make them perfect for orthopedic applications. However, the available CaPs possess a major drawback of slow bone formation rate resulting in a longer time for recovery of patients. Thus, this affects the psychological, physical and economic well-being of the patient and their family members. Electrical stimulation has been proven to enhance the osseous formation in different animal studies which in turn led towards the development of different piezoelectric devices and piezoelectric/biomaterial composites. Keeping these facts in mind, present work utilized the piezoelectric nature of Barium titanate (BT) into the different CaP compounds. The prime focus of this thesis is to enhance the electrical properties of CaP such that it helps to promote early osteogenesis. Furthermore, the minimally invasive surgery demands for the injectable self-setting CaP formulations whereas dense CaP scaffolds are most for the load-bearing applications. To address these applications, we carried out two different projects, first being injectable monetite based

piezoelectric bone cement and second sintered HA-BT piezobiocomposites. Interestingly, as far as our knowledge, no literature is available on the CaP bone cement with piezoelectric properties. Thus, the development of piezo- CaP bone cement is the first of its kind and signifies the novelty of this thesis.

Here, BT particles act as a source of electrical energy during normal physical loading conditions. The incorporation of BT into CaPs results in three major advantages. First, it improves the electrical properties (dielectric constant, piezoelectric coefficient) of the CaPs. Second, considering CaPs as a preferable cell-growing scaffold, BT incorporation enhances osteoblast cell activities and responses. Lastly, in case of CaP cement formulations, it increases the radiopacity such that the cement flow can be tracked under fluoroscopy and leakage can be avoided. The influence of ferroelectric barium titanate incorporation into sintered and self-setting CaPs scaffolds was studied in terms of physical, mechanical, chemical and biological properties. Additionally, the effectiveness of conventional sintering was compared with high-tech, capital-intensive spark plasma sintering (SPS).

The whole thesis is divided into three different chapters. The first chapter provides the overview on BT, self-setting CaP and sintered HA and studies on them. The second chapter deals with the monetite based bone cement and the last chapter describes conventionally sintered HA-BT. Both, bone cement and sintered HA-BT, samples exhibited desired mechanical and electrical properties. Moreover, they were not cytotoxic and helped in cell proliferation thus making them a possible candidate for different orthopedic, spinal-fusion and dental applications.

Dedicated to my family

Acknowledgements

I would like to express my special thanks of gratitude to my advisor Dr. Sarit B. Bhaduri for his continuous support, motivation, supervision, and guidance throughout my MS thesis. Without his mentoring, I would never have accomplished this work. I would like to appreciate the Department of Mechanical, Industrial and Manufacturing Engineering TA support. Furthermore, I would like to acknowledge the contributions made by my committee members Dr. Mehdi Pourazady and Dr. Matthew Franchetti towards the successful completion of my thesis. Also, I am grateful to Dr. Boren Lin and Mr. Bipin Gaihre for their help in biological studies. I would like to thank my fellow lab mates and friends in UT, especially Mr. Prabaha Sikder for the support and cooperation during my studies. Lastly, I wish to express my indebtedness to my family for all their encouragement and support towards my well-being.

Table of Contents

Abstract	iii
Acknowledgements	vi
Table of Contents	vii
List of Tables	xi
List of Figures	xii
List of Abbreviations	xiv
1. Calcium Phosphates and Piezoelectricity	1
1.1 Overview	1
1.2 Piezoelectric material: Barium Titanate	4
1.3 Compounds in CaO-P ₂ O ₅ system	6
1.4 Sintered Calcium phosphate bioceramics	8
1.4.1 Stages in Conventional Sintering	8
1.4.2 Studies on sintering of Hydroxyapatite	9
1.5 Self-setting Calcium phosphate cements	11
1.5.1 Studies on monetite cement	14
1.6 Components of the thesis	16
2. Smart injectable monetite based bone cement with piezoelectric properties	17
2.1 Introduction	17
2.2 Experimental	20

2.2.1 Materials	20
2.2.2 Sample Preparation	21
2.2.2.1 Premixed powder (PMP) preparation	21
2.2.2.2 BT cement samples preparation	22
2.2.3 Setting time	22
2.2.4 Mechanical Properties	23
2.2.5 Physical Characterizations	23
2.2.5.1 X-ray diffraction analysis	23
2.2.5.2 Fourier transform infrared spectroscopy analysis	23
2.2.5.3 Morphological observation	24
2.2.6 Simulated body fluid (SBF) immersion	24
2.2.7 Injectability	25
2.2.8 Washout Resistance Test	25
2.2.9 Biodegradation	25
2.2.10 In vitro cytocompatibility	26
2.2.10.1 WST-1 assay	26
2.2.10.2 Live and dead cell assay	27
2.2.11. Statistical analysis	28
2.3 Results	28
2.3.1 Setting Time	28
2.3.2 Mechanical Properties	29
2.3.3 Physical characterizations	29
2.3.3.1 XRD Analysis	29

2.3.3.2 FTIR Analysis	30
2.3.3.3 Morphological observation of cements	31
2.3.4 Simulated body fluid (SBF) immersion	33
2.3.5 Injectability	34
2.3.6 Washout Resistance test	34
2.3.7 Biodegradation	35
2.3.8 Cytocompatibility	36
2.4 Discussion	38
2.5 Conclusion	43
3. Conventionally sintered hydroxyapatite-barium titanate piezobiocomposites	44
3.1 Introduction	44
3.2 Experimental	46
3.2.1 Materials and sample preparation	46
3.2.2 Physical Properties	47
3.2.3 Mechanical Properties	48
3.2.3.1 Compressive Strength	48
3.2.3.2 Hardness and fracture toughness	48
3.2.4 Physical Characterizations	49
3.2.4.1 X-ray diffraction analysis	49
3.2.4.2 Fourier transform infrared spectroscopy analysis	49
3.2.4.3 Morphological observation	49
3.2.5 Bioactivity of samples in simulated body fluid (SBF)	50
3.2.6 In vitro cytocompatibility	50

3.3 Results	51
3.3.1 Physical and mechanical properties	51
3.3.2 Physical Characterizations	53
3.3.2.1 XRD analysis	53
3.3.2.2 FTIR analysis	54
3.3.2.3 Surface Morphology of sintered samples	55
3.3.3 Bioactivity of sintered samples	56
3.3.4 In vitro cytocompatibility	56
3.4 Discussion	57
3.5 Conclusion	60
4. Future Works	61
References	62

List of Tables

Table 1.1	Hydrated Calcium phosphate (low temperature).	7
Table 1.2	Desired properties of Injectable CaP bone cements.	13
Table 2.1	Information on incorporated Colloidal silica.	21
Table 2.2	Different smart CaP cement compositions.	22
Table 2.3	Chemical composition of 1.5 x t-SBF.	24
Table 2.4	Setting time for smart CPCs with various wt.% BT.	28
Table 3.1	Various compositions of sintering samples.	47
Table 3.2	Physical and mechanical properties of HA-x BT samples.	52

List of Figures

Figure 1-1 Literature on CaPs, sintered CaPs, and injectable CaP bone cements over last two decades (Web of Science database).	4
Figure 1-2 Crystal structure of cubic phase BT.	5
Figure 1-3 Ternary CaO-P ₂ O ₅ -H ₂ O system phase diagram at 25°C.	7
Figure 1-4 (a)Consolidation by superficial diffusion and formation of necks between grains (b) Consolidation by volume or grain boundary, diffusion (c) Coalescence and grain growth by grain boundary sliding.	9
Figure 2-1 Compressive Strengths of different compositions of smart CPCs.	29
Figure 2-2 XRD patterns of CPC with various wt.% BaTiO ₃ (‘■’ represents BT, ‘●’ represents monetite and ‘◆’ represents newberyite).	30
Figure 2-3 FTIR spectra of smart CPC formulation with varying wt.% BT.	31
Figure 2-4 SEM images of (a) CPC-0BT (b) CPC-10BT (c, f) CPC-20BT (d) CPC-30BT (e) CPC-40BT.	32
Figure 2-5 SEM images of (a)CPC-0 BT, (b, d) CPC-20 BT and (c) CPC-40 BT after 7 days immersion in 1.5 × SBF.	33
Figure 2-6 Injectability of smart CPC-x BT formulations where (a) x= 0 wt.% (b) x=10 wt.% (c) x= 20 wt.% (d) x= 30 wt.% and (e) x=40 wt.%.	34
Figure 2-7 Washout resistance test in SLS (a) CPC-0 BT (b) CPC-10 BT (c) CPC-20 BT (d) CPC-30 BT and (e) CPC-40 BT after 5 min.	35

Figure 2-8 Weight loss % of CPC-x BT samples in $1.5 \times$ SBF at different point of time.	35
Figure 2-9 OD values of OB-6 pre-osteoblast cells seeded in smart CPC-x BT formulations and HA after 24h and 72h, * refers to statistically different pair ($p < 0.05$).	36
Figure 2-10 Live and dead cell assay for the cells attached and proliferating along the surface of a) CPC-0 BT, b) CPC-20 BT, c) CPC-40 BT, and d) HA surface at day 5. The viable cells are indicated by the green fluorescence and dead cells by the red fluorescence. Scale $1000 \mu\text{m}$	37
Figure 3-1 HA-x BT sintered samples at 1200°C for 1h.	51
Figure 3-2 Cracks initiated from the corners of HA-20BT Vickers indent.	51
Figure 3-3 XRD analysis of sintered HA-x BT samples.	53
Figure 3-4 FTIR absorbance spectrum of sintered HA-x BT samples.	54
Figure 3-5 SEM images of sintered (a,b) HA (c,d) HA-20 BT (d,e) HA-40 BT.	55
Figure 3-6 SEM images of sintered (a) HA (b) HA-20 BT (c,d) HA-40 BT after 7 days immersion in $1.5x$ SBF.	56
Figure 3-7 Cytocompatibility of HA-x BT sintered samples after 1 and 7 days.	57

List of Abbreviations

α - MEM	Alpha minimum essential medium
α -TCP	Alpha Tricalcium Phosphate
β -TCP	Beta Tricalcium Phosphate
BT	Barium Titanate
Ca	Calcium
CaP	Calcium Phosphate
CDHA	Calcium Deficient apatite
CPC	Calcium Phosphate Cement
CT	Calcium Titanate
DCPA	Dicalcium Phosphate Anhydrous (Monetite)
DCPD	Dicalcium Phosphate Dihydrate (Brushite)
FTIR	Fourier Transform Infrared Spectroscopy
HA	Hydroxyapatite
HV	Vickers Hardness
Mg	Magnesium
MgO	Magnesium oxide
PMMA	Poly (Methyl Methacrylate)
PMP	Pre-mixed powder
PVA	Poly vinyl alcohol
SBF	Simulated Body Fluids
SEM	Scanning Electron Microscopy
SLS	Saliva Like Solution
SPS	Spark Plasma Sintering
TTCP	Tetracalcium phosphate
XRD	X-Ray Diffraction

Chapter 1

1. Calcium Phosphates and Piezoelectricity

1.1 Overview

Compounds in the $\text{CaO-P}_2\text{O}_5$ system, also called Calcium phosphates (CaPs), have been used in the field of orthopedics for over many decades. Their applications are wide-spread involving the fabrication of bone cement, biocompatible implants and coatings, scaffolds and even various composite materials [1-3]. CaPs with their similarity in chemical composition to bone minerals makes them the perfect candidate in the field of orthopedics [3-5]. One of the fascinating applications of CaPs is the self-setting nature of calcium orthophosphate cement. These setting characteristics have led to injectable CaP formulations for minimally invasive orthopedic surgery. However, the poor mechanical properties of self-setting CaP formulations limits them in load-bearing applications [4,5]. For load-bearing applications, dense CaPs are required because they exhibit much higher strength and toughness than the self-setting formulations. In most cases, sintering technique is implemented for fabrication of such dense products. The thermal treatment involved in sintering compacts the CaPs at a higher temperature but below its melting point to obtain a consolidated and densified product [3].

Fukada and Yasuda discovered the piezoelectric effect, the ability to develop electric charge by the certain material under mechanical stress condition, of bone in 1957 using the femur of man and ox. They proposed bone piezoelectric properties are associated with the crystalline micelle of collagen molecules as the piezoelectric effect was observed only when shearing force was applied to collagen [6]. Later, in 1964 they proposed the polarization or displacement of hydrogen bonds within the polypeptide chains of collagen crystals to be responsible for the origin of the piezoelectric effect [7]. Shamos and Lavine (1967) demonstrated piezoelectric effects in soft and hard tissues due to the presence of oriented fibrous proteins [8]. Furthermore, Anderson and Ericksson studied the nature and source of electrical properties of dry and wet bone when stressed. Under a fully hydrated condition, bone exhibited some piezoelectricity when it was mechanically stressed, and streaming potentials were observed to be the major source of these potentials [9]. Bassett and Becker (1962) postulated that electric potential influences osteoblast activities and the alignment pattern of macromolecules of the extracellular matrix. Also, bone ceases to display its stress potentials with the removal of the inorganic part [10]. When natural bone is mechanically deformed, it polarizes such that areas under compression are negatively charged while areas under tension are positively charged. For deformed bone, Bassett (1965) observed more enhanced bone growth around the negatively charged regions than positively charged ones [11]. These inherent piezoelectric potentials of bone assist in the bone development, maintenance, and fracture healing/ remodeling during normal physical activities [12-14]. To enhance the osseous formation and fracture healing, electrical stimulation, piezoelectric devices and bulk substrate/piezoelectric composites have been developed. With dc electrical stimulation Fredericks et al. reported significantly higher

gene expression corresponding to osseous formation [15]. A series of *in vivo* literature on the effect of electrical stimulation on interfacial strength from Park group are available [16-19]. The tensile strength at the interface between electrically stimulated calcium aluminate specimens and bone after 4 weeks of implantation in the rabbits' femurs were approximately twice when compared to non-stimulated control [16]. Higher the bone ingrowth, higher will be the interfacial strength. Even though the interfacial strength of stimulated samples was higher than control, the chemical assay revealed an insignificant difference in the quantity of bone growth within the implants and non-stimulated control [17]. The microstructural changes around implants created due to the electrical stimulation are responsible for the substantial increase in interfacial strength [18]. Furthermore, Park et al. also reported significant enhancement of interfacial strength between porous PMMA dental implants and oral tissues on the fourth premolar of dogs with electrical stimulation, however, if infection occurs the strength of control surpasses that of stimulated specimen [18,19]. A piezoelectric spinal fusion interbody device fabricated by Tobaben et al. delivered electrical stimulation from the natural loading and unloading of the spine [20]. Jianqing et al. implanted hydroxyapatite (HA) and polarized HA-Barium titanate (BT) ceramics in dog jawbones and observed earlier osteogenesis around HA-BT implants as compared to HA [21]. Therefore, the integration of electrical properties to orthopedic implants can be beneficial as they promote the recovery of the patient.

To identify the significance of the present work, a literature search was carried out in the Web of Science database using three different keywords 'Calcium phosphate and bioceramics', 'Sintering calcium phosphate and bioceramics' and 'Injectable calcium phosphate and bone cement'. With the development of self-setting CaP formulations by

LeGros et al. and Brown and Chow in the 1980s, CaPs began to gain the attention of many researchers. Before 1990, the topic of CaPs was in a nascent stage and began to achieve popularity after 1995. Figure 1-1 presents the total number of publications on respective topics for over the last two decades.

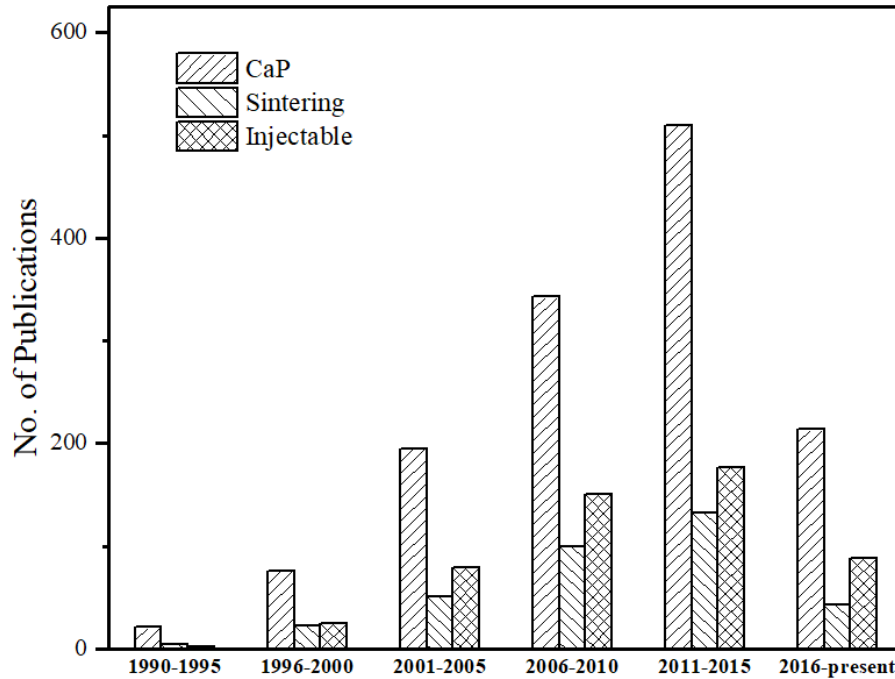


Figure 1-1: Literature on CaPs, sintered CaPs, and injectable CaP bone cements over last two decades (Web of Science database)

1.2 Piezoelectric material: Barium titanate

Barium titanate or BaTiO_3 (BT) is a ferroelectric material with a perovskite structure and is described with a formula ABX_3 . The molecular weight and density of BT is 233.19 g/mol and 6.02 g/cm³ in the solid state respectively. It has a melting point of 1625°C. The piezoelectric constant value of BT (d_{33}) is approximately 191pC/N. This high piezoelectric property makes BT as a suitable candidate for an enhancement of osseous formation even in a complex physiological environment [22]. The high permittivity ϵ_r of BT was

discovered in 1943 and was employed in ceramic capacitor manufacturing afterwards. The permittivity of BT depends strongly on the grain size a and has a value of approximately 1500-2000 at room temperature for coarse-grained pure BT where $20 \leq a \leq 50 \mu\text{m}$. However, for grain sizes less than $1 \mu\text{m}$, the ferroelectric structure of BT changes resulting in a decrease in the dielectric constant value [23]. The crystal lattice structure of BT can be tetragonal, orthorhombic, rhombohedral, and cubic. The perovskite BT structure is formed with Ba^{2+} ions at the corners of a cube, O^{2-} ions at the centers of the six faces, and Ti^{4+} ions at the center of an octahedral structure formed by oxygen ions [23,24]. BT exhibits paraelectric cubic structure at elevated temperature but reorganizes into a ferroelectric tetragonal phase below 125°C [24].

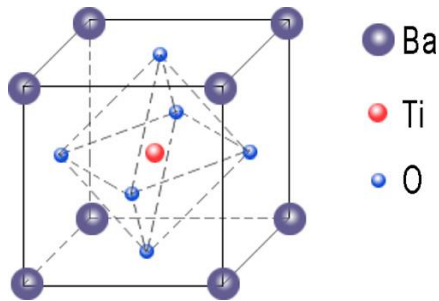


Figure 1-2: Crystal structure of cubic phase BT [24]

Literature is available on BT as a potential candidate for a piezoelectric biocomposite. In the early 1980s, *in vivo* feasibility of polarized BT as piezoelectric ceramic implants was carried out by Park group such that the necessity of power pack during the electrical stimulation can be eliminated. Moreover, with the increase in the implantation period from 16-day to 86-day, more bone ingrowth and higher tissue /implant occur such that better load transfer and higher output voltage were obtained [25]. The BT ceramic implants subjected to heat at 1430°C maintained *in vitro* mechanical stability (compressive strength) even when they were immersed in physiological saline for 4 weeks. The modulus of rupture

and compressive strength of dense polycrystalline BT were reported to be 85.5 MPa and 486 MPa respectively [26]. Later in 1981, Park et al. published a paper on *in vivo* BT ceramic implants studies on the cortex of midshaft region of the femora of dogs. No significant difference between polarized and non-polarized BT implants in interfacial strengths and amount of mineralized ingrowth was observed. However, BT ceramic implants displayed high biocompatibility as 80% of pores were filled with mineralized tissues within 99 days [27]. A research performed by Beloti et al. [28] studied *in vitro* human osteoblast cells responses of poly(vinylidene-trifluoroethylene)/barium titanate composite membrane. In addition to better biocompatibility, they observed bone-like nodule formation of this novel membrane when compared with the expanded polytetrafluoroethylene (control) membrane. Furthermore, Dubey et al. (2015) confirmed the non-toxicity effect of BT as no trace of injected HA-BT particles or signs of inflammation were spotted in the vital organs after 7 days of *in vivo* study on mice knee joint [29]. Y.J. Park et al. demonstrated improved *in vitro* bioactivity of negatively charged BT surfaces as compared to positively charged surfaces [30].

1.3 Compounds in CaO-P₂O₅ system

The liquid-solid phase equilibria of acid-base reactions influence the compositional and microstructural relationships among different CaPs. To have a better understanding of mechanisms and kinetics of hydroxyapatite formation during dissolution process of CaPs, the compositional relationships in a ternary CaO-P₂O₅-H₂O system can be a reliable tool. Brown [31] developed a ternary phase diagram at 25°C and atmospheric pressure condition by plotting the fifth roots of calcium phosphate concentrations as mole fractions of CaO or

P₂O₅. Figure 2-3 shows ternary CaO-P₂O₅-H₂O phase diagram consisting of stable CaP phases more basic than Ca(H₂PO₄)₂.

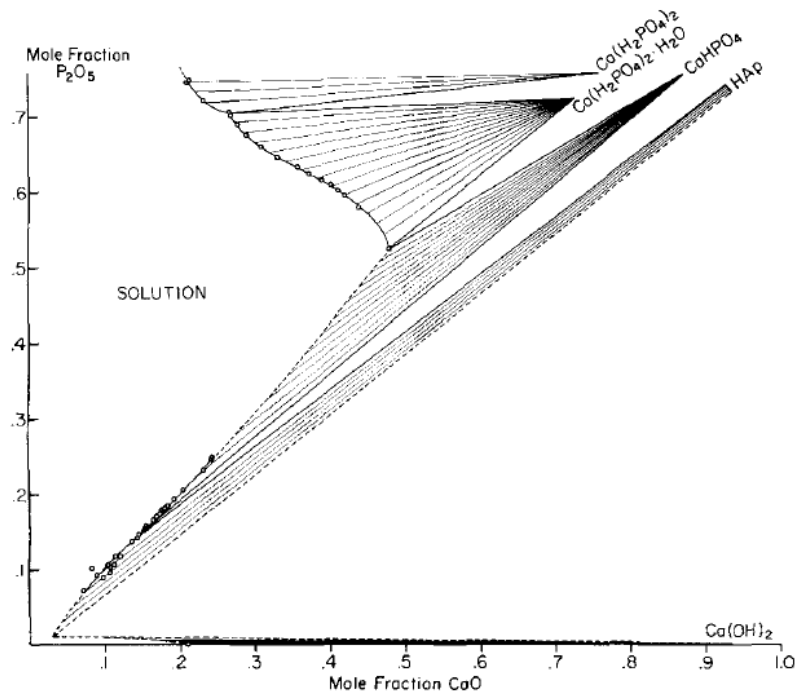


Figure 1-3: Ternary CaO-P₂O₅-H₂O system phase diagram at 25°C [31]

Table 1.1: Hydrated Calcium phosphate (low temperature)

Ca(H ₂ PO ₄) ₂	Monocalcium phosphate anhydrous (MCPA)
Ca(H ₂ PO ₄) ₂ • H ₂ O	Monocalcium phosphate monohydrate (MCPM)
CaHPO ₄	Dicalcium phosphate anhydrous (DCPA)
CaHPO ₄ • 2H ₂ O	Dicalcium phosphate dihydrate (DCPD)
Ca ₁₀ (PO ₄) ₆ (OH) ₂	Hydroxyapatite (HA)
Ca _{10-x} (HPO ₄) _x (PO ₄) _{6-x} (OH) _{2-x} (0 < x < 1)	Calcium-deficient hydroxyapatite (CDHA)

1.4 Sintered Calcium phosphate bioceramics

The term ‘sintering’ was coined in the 1800s and used commonly after mid- 1900s. Sintering is defined as a thermal treatment process for bonding particles into a coherent, predominantly solid structure via mass transport events on the atomic scale [32]. Sintering techniques can be broadly categorized into conventional pressureless sintering and non-conventional techniques. However, non- conventional sintering techniques can be two-step sintering, liquid phase sintering, hot pressing, hot isostatic pressing, ultrahigh pressure, microwave and spark plasma sintering. Recently spark plasma sintering technique has been topic of high interest. SPS involves heating of initial powder samples via applied electric current and compressing the powder simultaneously within a die. Faster heating and heat transfer rate of this technique accounts for the reduced sintering temperature to reach consolidation levels and lowers processing/holding time [3,33]. Therefore, SPS is a better choice where crystallization phenomenon, grain growth, and/or phases decomposition is a problem [33] and yet SPS is not suitable for mass production as they are capital intensive and requires expertise manpower. Nonetheless, conventional sintering is easy, cheap process and feasible for mass production.

1.4.1 Stages in Conventional Sintering

Conventional Pressureless sintering of HA occurs in three sequential stages. The first stage lasts up to a relative density of approximately 65% of theoretical value and involves grain weld resulting interparticle neck formation and growth (Figure 1-4(a-b)). During this initial stage light or no densification can be observed. The initial powder consolidation is due to superficial diffusion. The intermediate stage is a major part of sintering where densification occurs via shrinkage of pores. A relative density of approximately 90% is achieved at the

end of the intermediate phase. For HA, shrinkage begins at around 750°C and maximum sintering rate occurs at around 1050°C. In the final stage, the isolated pores formed at the end of the second stage disappears completely such that a fully or nearly dense ceramics is obtained. Grain boundary migration is pinned by open pores during intermediate stage while this phenomenon is drastically reduced in case of the final stage. This leads toward the grain growth during the final stage of sintering process [3]. The schematic diagram of sintering process is shown in Figure 1-4.

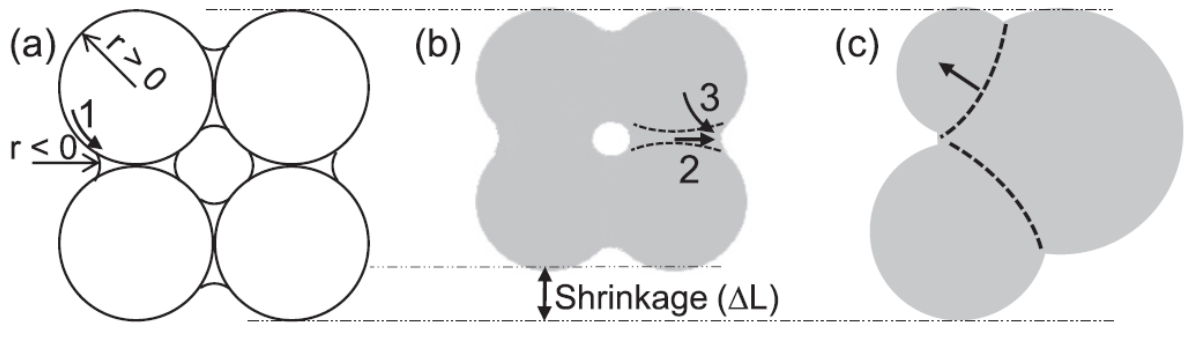


Figure 1-4: (a) Consolidation by superficial diffusion and formation of necks between grains (b) Consolidation by volume or grain boundary diffusion (c) Coalescence and grain growth by grain boundary sliding [3].

1.4.2 Studies on sintering of Hydroxyapatite

Similarity of HA with bone minerals have led researchers towards their studies on physical, chemical and biological properties, different synthesis techniques and possible scopes of applications. A research performed by Akao et al. on polycrystalline HA powder pressed at 60-80MPa followed by conventional sintering at different temperatures (1150,1200,1250 and 1300°C) for 3h showed maximum compressive, flexural and static torsional strengths exist at 1300°C [34]. Karimzadeh et al. investigated mechanical and tribological properties of a pressureless sintered commercial HA powder using

nanoindentation and nanoscratch tests. The results showed increase in hardness with increase in sintering temperature up to 1300°C and decreases afterwards. In addition, the maximum Young's modulus and scratch resistance were obtained at 1200°C and 1300°C respectively [35]. As cold isostatic pressing (CIP) improves uniformity in density and homogeneity in microstructure of final ceramics, Heidari et al. prepared HA samples by CIP method and sintered them at different temperatures. They also reported increase in relative density and hardness with increase in sintering temperature up to 1300°C with a maximum compressive strength at 1200°C [36]. Furthermore, Cuccu et al. studied the consolidation behavior of three commercially available HA using SPS technique. This study revealed that the use of refined grains with relatively small size particles and high purity HA powders results in a fully dense product at 900°C when no secondary phases was present. However, the optimum sintering conditions for large powder particles or finer ones with secondary phases demand for higher temperature levels as high as 1200°C leading to coarser microstructures and/or significant amount of β -TCP formation in the final products [37]. When comparing effects of sintering time and temperature on nano-sized HA powders, Monmaturapoj and Yatongchai concluded sintering temperature to have more prominent effect on grain size, density and strength [38]. Maidaniuc et al. studied silver as sintering additive and silver was reported to show a positive effect in sintering, resulting better consolidation of green body and locally contributing to wetting and relieving of ceramic particles [39].

More recently, for the last few decades, attempts are being made for the improvement of the mechanical properties such as fracture toughness, electrical, dielectric, piezoelectric properties and biological properties of sintered HA composites. Bellucci et al. developed

an innovative HA/bioactive glass composites via SPS technique with controlled bioactivity and dissolution rate by varying volume fractions of constituents [33]. Remarkable efforts on the development of piezobiocomposites HA-BT /HA-CT implementing SPS technique are available from Dubey and Basu research groups. The addition of CT to HA promotes the fracture toughness of piezobiocomposites as CT grains account for the crack tip-twin interaction [40]. HA-40wt.% CT demonstrated highest fracture toughness [40] while HA-80wt.% CT showed significantly higher dielectric, AC conductivity [41] than lower CT content composites and early stage neo bone formation [42] than HA composites. Regarding HA-BT piezobiocomposites, HA-40 wt.% composites showed a close resemblance to functional properties such as mechanical, dielectric and electrical properties of natural dry bone [43]. On the other hand, porous nanophase HA-25 vol.% BT piezobiocomposites exhibited acceptable mechanical and electrical properties [14].

1.5 Self-setting Calcium phosphate cements

In vivo animal experiment using CaP was performed for the first time in 1920. Later in 1951, the efficacy of HA as a bone substitute was identified in rat and pig subjects. Moreover, the discovery of self-setting (self-hardening, self-curing) behavior of calcium orthophosphates by LeGros et al., Brown and Chow in early 1980s unleashed a whole new level of CaP applications in orthopedics, dental and tissue engineering [4,5]. The self-setting formulation comprises two phases namely, powder phase and liquid phase. After mixing calcium orthophosphate powder with the liquid phase, a moldable, viscous paste is formed which hardens within few minutes. The liquid phase can be distilled water, phosphate buffer solution, aqueous solutions of sodium orthophosphates, ammonium

orthophosphates, citric acid and its salts, sodium silicate, soluble magnesium orthophosphates, chitosan lactate in lactic acid and so on [5]. The self-setting calcium orthophosphate putties can be directly filled into defect sites with either hand or injection and can be molded into the desired shape along with the advantage of minimally invasive surgery. However, the heat liberation during their setting has been a major drawback as they may cause in-site tissue inflammation. Therefore, to overcome this exothermicity problem, a novel microwave-assisted approach has been developed by our research group. Here, the setting reaction is temporarily stopped with microwave irradiation and later resumed by adding a liquid phase without any heat liberation [44].

All the self-setting CaP formulations are non-Newtonian fluids such that their viscosity depends on shear rate or shear rate history. Biomedically applicable CaP formulations demands for good injectability, sufficient viscosity, and satisfactory cohesion. The liquid-to-powder ratio (L/P) plays a crucial role in determining injectability and bioresorbability of cement formulation so proper attention should be given while selecting L/P ratio [3,4]. The characteristics of ideal injectable CaP bone cement for orthopedic, dental and spinal-fusion applications are listed in Table 1.2 [45,46].

Upon admixture of powder phase with a liquid phase, all CPCs set into two major end products: a precipitated poorly crystalline HA or CDHA at $\text{pH} > 4.2$ and Dicalcium phosphate dehydrate (DCPD) or brushite at $\text{pH} < 4.2$. Thus, the commercially available CPCs can be classified into either apatite cements or brushite cements. The first CaP cement fabricated by Brown and Chow is a classic example of apatite cement with tetracalcium phosphate (TTCP) and DCPA in an aqueous suspension at L/P ratio of 1:4 to form poorly crystalline HA [4,5]. Apatite cement can be either conventional formulation

comprising TCP and/or TTCP as powder phases or single component formulation contains K- and Na- containing CDHA [47,48]. The solubility kinetics of apatite cements are similar to bone minerals as they are relatively insoluble at neutral pH, but their solubility raises with pH drop [4,49].

Table 1.2: Desired properties of Injectable CaP bone cements

- Absence of toxicity
- Easy preparation, injectability and handling
- Adequate radiopacity to allow tracking of cement flow under fluoroscopy
- Working time within the range of 6-10 min
- Setting time of about 15 min
- Appropriate cohesion such that paste sets without disintegration
- Appropriate mechanical properties for immediate reinforcement, the value should be comparable to those of healthy cancellous bone
- Excellent osteoconductivity, osteoinductivity, biocompatibility and bioactivity
- Appropriate resorption rate such that the rates of degradation CaP formulation and growth of neo-bone formation are comparable
- Sufficient micro- and macro-porosity
- Reasonable cost

Brushite cement was discovered by Mirtchi and Lemaître, and Bajpai et al. in 1987 [5]. Mirtchi and Lemaître composition consist of a mixture of β -TCP/monocalcium phosphate monohydrate(MCPM) with water. Later in 1989, Mirtchi et al. investigated the effect of

aging above 40°C and 100% relative humidity and reported their detrimental effect on mechanical properties of cement [50]. Brushite cements mainly consist of an alkaline calcium source, acidic phosphate source and water along with some additives to enhance their setting time, mechanical properties and handling. TCP, TTCP, calcium oxide, calcium silicate and nanocrystalline HA has been used as an alkaline source. Whereas phosphoric acid, MCPM, monocalcium phosphate anhydrous (MCPA), sulfuric acid and citric acid has been used in the fabrication of brushite cement [51]. When compared to apatite cements, brushite formulations can initially be liquid but within a short period of time hardens into solid [52,53]. Most of the available apatite and brushite bone cements have TCP or TTCP as starting materials and involves high temperature around 1200°C for their synthesis, thus demanding for a capital-intensive manufacturing process for quenching them to room temperature [54]. These disadvantages can be resolved with a different phase of dicalcium phosphate: monetite cements as they are can be produced at low-temperature conditions.

1.5.1 Studies on monetite cement

The high aqueous solubility of Dicalcium phosphate anhydrous (DCPA) or monetite (CaHPO_4) at and around physiological pH as compared to all other biocompatible CaP phases led Desai et al. (2007) towards the development of the very first orthopedic cement based on monetite [54]. Monetite cement can be synthesized by reacting calcium ions sources such as calcium hydroxide or calcium nitrate with concentrated phosphoric acid solutions such that the pH lies within the range of 2.5-4.2 [51,54]. Furthermore, thermal hydrolysis of brushite cements, and dicalcium phosphate precipitation at a limited water and rich in alcohol groups condition result in monetite formation [51,55]. Cama et al.

developed a novel technique to fabricate micro- and macroporous monetite cement by incorporating sodium chloride into β -TCP and MCPM [56].

In vivo studies on rabbit and human subjects using monetite bioceramics and granules formed by thermal conversion of preset brushite cement discovered the faster resorption and augmented bone growth than brushite and bovine hydroxyapatite respectively [57,58]. Tamimi et al. (2008) reported significant improvement in bone healing when monetite granules were incorporated into the rabbit calvaria bone defects [59]. Later in 2009, Tamimi et al. also designed monetite 3D printed blocks and onlay grafts for vertical bone augmentation. They observed 42% of monetite resorbed and 43% of neo-bone formation within the implants after 8 weeks [60]. Montazerolghaem et al. revealed the osteoclasts to be highly responsible for resorption of monetite cement [61]. Brushite cements convert into stable hydroxyapatite resulting in their poor resorption rate whereas monetite cements, on the other hand, retain their crystalline phase even when they are implanted *in vitro/ in vivo* such that the higher resorption rate can be observed on monetite than brushite cements [62,63].

Our research group has been continuously exploring the monetite cements for a decade. The hydrolysis of monetite in Alpha minimum essential medium (α -MEM) and simulated body fluid (SBF) revealed the transformation of monetite into carbonated apatite. However, in the presence of chitosan in monetite composite the transformation was altered such that the rapid rate of transformation was observed in SBF as compared to α -MEM [64]. Furthermore, nanoporous electrospun PLA/monetite nanocomposite fibers with a uniform distribution of monetite particles were fabricated [65]. Several works have been carried out to improve the setting time, mechanical properties and bioactivity of monetite cement by

incorporation of carbon nanotubes, chitosan and colloidal nanosilica [66-69]. This present work is a very first of its kind as it deals with the enhancement of electrical properties of monetite cement.

1.6 Components of the thesis

This thesis is arranged with a prime focus on the application of CaPs. The chapter 2 is comprehensive and describes a novel approach to develop an injectable monetite base piezo-bone cement with enhanced electrical properties. Different physical, mechanical, electrical and biological properties of cement have been tested and the results are presented in this chapter. On the other hand, the load bearing application of CaP was studied with sintered HA. The piezobiocomposites HA-BT were synthesized using conventional sintering furnace and the sintered samples were tested for various properties. All the results corresponding to sintered composites are allocated to Chapter 3.

Chapter 2

2. Smart injectable monetite based bone cement with piezoelectric properties

2.1 Introduction

Approximately half of the world population experience at one least bone fracture during their lifetime [5]. The loss of bone tissues from fracture and the presence of an intersegmental gap exceeding 2.8mm might cause a delay in the fracture consolidation, pseudoarthrosis or even false union [70]. Since human and animal derived bone graft substitutes are highly susceptible to disease transmission, synthetic substitutes are receiving more attention [71]. Calcium phosphate cements (CPCs) are self-setting, moldable synthetic implants with excellent bioactivity, biocompatibility, biodegradability and osteoconductivity. Thus, CPCs are emerging as potential modern therapeutic bone substitutes with a wide range of scope in orthopedic, dental, spinal, oral, maxillofacial and craniofacial applications [4, 5,72]. Commercial CPCs can be mainly classified as apatite and brushite (DCPD) cement [4,5]. Owing to its fast degradation rate, DCPD transforms into a stable apatite phase after *in vivo* implantation [73]. However, in biomedical applications, the release of orthophosphoric acid during the degradation of DCPD to apatite might causes a certain degree of tissue inflammation [5]. On the other hand, monetite

[dicalcium phosphate anhydrous (DCPA)] with its chemical compositional similarity to DCPD, exhibits a much more stable degradation rate and does not transform into hydroxyapatite (HA), thus increasing the chances of higher bone volume formation [5,56,57,74]. This makes DCPA a perfect synthetic bone cement candidate. Our group has sustained research thrust in fabricating bone cement, especially DCPA and is also one of the major phases in the CPC cement formulation of the present study [64,66-69].

Natural bone possesses electrical properties namely piezoelectricity [6-11,22,75-79], ferroelectricity [80], pyroelectricity [81], and electrical conductivity [82]. The electrical properties arise due to the presence of collagen and ionic fluid movement in the bone structure [40,83]. Piezoelectricity is the ability of a material to develop electric charges under pressure conditions and such effect assists in bone development, maintenance and fracture healing [12-14]. Encapsulating piezoelectric material within orthopedic implants can harvest electrical energy from mechanical energy during normal physical activities. This electrical energy can be utilized for a broad range of biomedical purposes [12]. A relevant question which arises in this context is whether CPCs possess similar piezoelectric properties like natural bone.

Barium titanate or BaTiO_3 (BT) is one of the most extensively studied compound from the group of ferroelectric materials with perovskite structure (ABX_3). Owing to its high dielectric constant and piezoelectric properties, BT has found a wide range of applications not only in electronics but also in the biomedical industry [13,84]. BT nanoparticles have been used in nanomedicine, nonlinear imaging purposes, drug delivery, tissue engineering and innovative bio-stimulation approaches [84]. The piezoelectric constant of BT (d_{33}) is approximately 191pC/N which makes it favorable for enhancement of bone/osseous

formation even in a complex physiological environment [83]. In early eighties, Park et al. reported that dense sintered BT implants are able to stimulate bone growth in dog femurs [25,27]. The implants were stable with the dog for several months and did not cause in cytotoxicity. These initial experiments showed the effective applications of piezoelectric BT in orthopedics. Two decades later in 1997, Jianqing et al. developed HA-BT composites by using conventional sintering and polarized them before putting them into dog jawbones. The results showed one-week earlier bone formation around HA-BT implants as compared to undoped HA [21]. Dubey et al. and Prakasam et al. fabricated BT infused HA piezobiocomposites via multi and single-stage spark plasma sintering (SPS) respectively and the results yielded good biomechanical and electrical properties [43,83]. Furthermore, when surface charge was generated by electrical poling on such HA-BT composites, higher cell proliferation was observed on the negatively charged surfaces [13]. *In vivo* studies also revealed no vital organ inflammation after 7 days when HA composites containing 40 wt.% BT was infused into the right knee joint of mice using an intra-articular injection [29]. Even porous nanophase HA-BT composites were proven to be potential candidates in fabrication of piezoelectric orthopedic implants [14]. However, BT have been hardly considered as a filler in bone cements.

R.G.Carrodeguas et al. prepared a partially biodegradable and injectable bone cement consisting of poly(methyl methacrylate) (PMMA) matrix infused with BT or strontium titanate (SrTiO_3) [70, 85]. To the best of our knowledge no efforts have been made to introduce piezoelectric materials into CPCs. The present study is one of the first of its kind which focusses on fabrication of smart injectable CaP cement for orthopedic and spinal-fusion. The “smart” aspect of the compositions is achieved by incorporating piezoelectric

materials i.e. BT in the monetite cement. As described previously, all research have focused mainly on sintered HA-BT scaffolds. However, injectable bone cement is much favorable for minimally invasive orthopedic surgery. Apart from enhancing mechanical and electrical properties, incorporation of radiopaque BT into injectable bone cement is highly advantageous as it will increase the visibility of CPCs under X-rays. Thus, during injection, the cement flow can be easily monitored under fluoroscopy to avoid leakage. The present work reports the development of novel technique for smart injectable electroactive biomaterial: CPCs augmented with BT and investigates their physical, mechanical, electrical properties and their cytocompatibility *in vitro*. We expect that BT incorporation would enhance the electrical properties of CPCs which would in turn help in enhanced bone formation at the defect site.

2.2 Experimental

2.2.1 Materials

Barium titanate (IV) (BaTiO_3 , 99.5%, particle size $\leq 2\mu\text{m}$) and colloidal silica were procured from Sigma-Aldrich and used without further modification. The detailed information of colloidal silica is presented in Table 2.1. Calcium hydroxide ($\text{Ca}(\text{OH})_2$, >95%), magnesium hydroxide ($\text{Mg}(\text{OH})_2$, 95%), sodium bicarbonate (NaHCO_3 , >99.7%) and magnesium oxide (MgO , 98%) from Fischer Scientific and sodium tetraborate decahydrate ($\text{Na}_2\text{B}_2\text{O}_7 \cdot 10\text{H}_2\text{O}$, > 99.5%) from Alfa Aesar were used for the preparation of the cement samples.

Table 2.1: Information on incorporated Colloidal silica

Product	Concentration	Surface area	pH	Density
LUDOX® HS-40 colloidal silica	40 wt.% suspension in H ₂ O	~ 220m ² /g	9.8	3gm/mL at 25 ⁰ C

2.2.2 Sample Preparation

2.2.2.1 Premixed powder (PMP) preparation

Preparation of CaP cement (CPC) samples requires a kind of setting solution and premixed powder (PMP). The setting solution was prepared by diluting 78mL of o-phosphoric acid (H₃PO₄, 85%) with 12mL of DI water placed in an ultrasonic bath, followed by the addition of 12g sodium bicarbonate. The preparation of setting solution is critical in material preparation as it influences the setting time of the fabricated bone cement. For a controlled reaction rate, 3g of NaHCO₃ was added with an interval of 30 sec. The ultrasonic bath was kept running until the setting solution became clear and then was stored in a tightly capped glass bottle. To prepare PMP, initially, 55.2g of Ca(OH)₂ and 13.8g of Mg(OH)₂ were mixed homogenously in a household mixer (KitchenAid 325W motor). After few minutes of mixing, the setting solution was slowly poured into the mixer bowl and allowed to run for another 2 minutes. The mixer was kept running at the lowest speed for the whole time. At the end of 2 minutes, formed chunks were taken out into a glass bowl and placed immediately inside a household microwave (Panasonic, 1250W) and irradiated at 10% power level (Level 1) for 6 minutes. This microwave cycle was repeated several times until the chunks became rock-hard. Finally, the rock-hard cement precursors were grinded into powder using mortar and pestle and PMP fine powders ($\geq 250\mu\text{m}$) was obtained by sieving it through U.S.A. Test Sieve (ASTM E11 specification).

2.2.2.2 BT cement samples preparation

$\text{Na}_2\text{B}_2\text{O}_7 \cdot 10\text{H}_2\text{O}$ (4 wt. % of PMP), MgO (5 wt. % of PMP) and varying amounts of BT (0, 10, 20, 30, 40 wt. % of total powders) were added to 5g PMP and mixed homogeneously. Colloidal silica (liquid) was added to the powder mixture phase using a pipette such that the liquid to powder ratio was maintained constant at 0.35 mL/g. The specimen name along with its compositions are presented in Table 2.2. After addition of colloidal silica, the mixture was vigorously mixed for 60sec using a mortar and pestle. Finally, the formed putty was put into cylindrical molds and prepared for various characterizations.

Table 2.2: Different smart CaP cement compositions

Cement	PMP (g)	Borax (g)	MgO (g)	BaTiO₃ (g)	Colloidal silica (mL)
CPC-0 BT	5	0.20	0.25	-	1.910
CPC-10 BT	5	0.20	0.25	0.545	2.100
CPC -20 BT	5	0.20	0.25	1.090	2.290
CPC -30 BT	5	0.20	0.25	1.635	2.480
CPC -40 BT	5	0.20	0.25	2.180	2.670

2.2.3 Setting time

The initial and final setting time of the smart CPC-xBT (x = wt. % of BT) cements were obtained using Gillmore needle method (ASTM C266-89). Light and thick needle measures the initial setting time while heavy and thin needle measures the final setting time. The initial and final setting times were recorded when the needle left an indentation

depth less than 1 mm on the sample surface. Additionally, respective setting times were measured at an interval of 15 sec.

2.2.4 Mechanical Properties

Smart CPC-xBT samples with dimensions, \varnothing 12.5mm and height 7mm, were prepared for mechanical properties evaluation. Cement samples were allowed to set for 24h at room temperature. Compression strength testing was carried out on a universal testing machine with the application of 50 kN uniaxial load cell (model 5569, Instron, Norwood, MA, USA). As per the protocol of the American dental association i.e. $0.75 \pm 0.25 \text{ mm min}^{-1}$, the crosshead loading rate of 0.5 mm min^{-1} was set [66].

2.2.5 Physical Characterizations

2.2.5.1 X-ray diffraction analysis

X-ray diffraction analysis (XRD, Ultima III; Rigaku, The Woodlands, TX) with monochromated Cu $K\alpha$ radiation (44KV, 40mA) was used to study the phases present in the as-prepared CPC-xBT samples over 2θ range of $10-60^\circ$. MD JADE software 2010 (MDI, Livermore, CA, USA) was employed to identify the respective phases.

2.2.5.2 Fourier transform infrared spectroscopy analysis

The functional groups present within the samples were identified with Fourier transform infrared spectroscopy (FTIR, UMA-600 Microscope, Varian Excalibur Series, Digilab, Holliston, MA, USA) using an ATR diamond crystal. 256 scans were performed on each sample within the range of 4000 to 700 cm^{-1} .

2.2.5.3 Morphological observation

Surface morphology of the samples were examined using scanning electron microscope (SEM, S-4800, Hitachi, Japan). All the samples were mounted on SEM stubs with a copper conducting tape and sputter coated for 90 secs before conducting SEM study.

2.2.6 Simulated body fluid (SBF) immersion

Smart CPC-x BT samples pellets ($\text{\O} 6.4 \times 3 \text{ mm}^3$) were immersed into tightly capped 50 ml autoclaved bottles filled with 30 ml 1.5 x t-SBF. The detailed composition of $1.5 \times \text{t-SBF}$ is shown in the Table 2.3 [86]. The bottles containing the SBF immersed samples were placed in a water bath at 37°C for 7 days. Moreover, the SBF was replenished every other day in order to keep the ionic compositions constant. After the time period, samples were cleaned under flowing distilled water and thoroughly dried in an air-convection furnace at 60°C for further characterization under SEM.

Table 2.3: Chemical composition of 1.5 x t-SBF

Order	Reagent	Weight (g per L)
1	NaCl	9.8184
2	NaHCO ₃	3.4023
3	KCl	0.5591
4	Na ₂ HPO ₄	0.2129
5	MgCl ₂ ·6H ₂ O	0.4574
6	1M HCl	15mL
7	CaCl ₂ ·2H ₂ O	0.5513
8	Na ₂ SO ₄	0.1065
9	TRIS	9.0855
10	1M HCl	50mL

2.2.7 Injectability

Colloidal silica was added to $\text{Na}_2\text{B}_2\text{O}_7 \cdot 10\text{H}_2\text{O}$, MgO and varying amounts of BT to form putty-like materials which were put into syringes (BD Biosciences, San Jose, CA) with a nozzle diameter of 1.36 mm. The nozzle diameter used in the present work lies between gauge 15 (1.449 mm) and gauge 16 (1.291 mm) and is smaller than the actual needle size used in clinical cement injection [87]. After loading the putty, the plunger of the syringe was propelled manually to examine the injectability of the as-prepared CPC- x BT cement samples. The samples were considered to have certifiable injectability if the cement did not remain inside the syringe during injection.

2.2.8 Washout Resistance Test

As per Takagi et al. protocols, different composition of cement pastes were prepared, loaded into syringes and then immediately injected into Saliva-like Solution(SLS) at 37°C even before the initial setting time [88]. Immediate injection of cement mimics the real-time orthopedic application and thus is a pragmatic evaluation. SLS was prepared using 1.2 mmol/L calcium chloride (CaCl_2), 0.72 mmol/L monopotassium phosphate (KH_2PO_4), 30 mmol/L potassium chloride (KCl), 50 mmol/L HEPES buffer (N-2-hydroxyethyl-piperazine-N'-2'-ethane sulfonic acid) and finally its pH was adjusted to 7 with 0.1 mol/L NaOH. The sample was considered to pass the washout resistance test if it did not visibly disintegrate in the SLS for 5 minutes.

2.2.9 Biodegradation

In order to study the *in vitro* biodegradation rate of smart CPC-x BT samples ($\text{Ø } 12.5 \times 7 \text{ mm}^3$), $1.5 \times \text{t-SBF}$ solution was used as the medium. As per the Wu et al. protocol, cement

samples, after they have set for 24h, were immersed in glass bottles containing $1.5 \times t$ -SBF. The bottles were then placed in a water-bath shaker which maintained 37°C and 100 rpm. The weight-to-volume ratio of the test specimens were also maintained to be 0.2gm/ml [89-91]. For over a time span of 7 days, each and every day the samples were retrieved from the SBF solution, cleaned in deionized water, dried at 60°C for 2h and weighed for any weight loss. The dried coupons were re-immersed into fresh $1.5 \times t$ -SBF solution with repetition of the above-mentioned steps. The biodegradation rate of the coupons at various point of time was calculated using the equation 2-1.

$$\text{Weight loss} = (W_i - W_d) / W_i \times 100\% \quad (2-1)$$

Where, W_i represents initial coupon weight, and W_d represents dried coupon weight after degradation.

2.2.10 In vitro cytocompatibility

2.2.10.1 WST-1 assay

OB-6 pre-osteoblast cell line and water soluble tetrazolium (WST-1) assay were used to study the cytocompatibility of the smart cement samples. This is a colorimetric assay based on the conversion of stable tetrazolium salt into soluble formazan by the cellular mechanism that occurs at the cell surface. Hence, the amount of formazan detected directly relates to the number of metabolically active cells. For this assay, sample pellets ($\emptyset 6.4 \times 3 \text{ mm}^3$) were incubated in complete culture medium for 24 h at 37°C and 5% CO_2 in a 24 well plate, following the extraction ratio of $3 \text{ cm}^2/\text{ml}$. In a 96-well plate, 10,000 cells/well were plated and incubated at the same conditions for 24 h. After 24 h, the culture medium on the cell plated 96-well plate was replaced with 100 μl of the extracted or conditioned medium (the medium which contained the specimens for 24h). The cells were further

cultured in the conditioned media for a period of 24 h or 72h at 37 °C and 5% CO₂. At specific time points, 10µl (1:10 ratio) of WST-1 reagent was added to wells containing cells/medium and incubated for 4 h under the same conditions. After 4 h, the formation of water soluble formazan was detected at 450 nm using SpectraMax 190 microplate reader (Molecular Devices, USA).

2.2.10.2 Live and Dead cell assay

The viability of pre-osteoblasts (OB-6) attached to the samples was imaged using Cytation 5 cell imaging multi-mode reader (BioTek, USA) after staining them with Live/Dead cell viability kit (Thermofisher Scientific, USA) at day 5. The samples were first kept under the UV light for 15 min followed by the incubation with complete cell culture media for 1 h at 37°C and 5% CO₂. The OB-6 cells harvested from the cell-culture dishes were then seeded onto the top of the samples at 30,000 cells/sample. In order to allow the proper attachment of the cells to the sample, 200 µl of cell suspension containing 30,000 cells was first added to the samples and incubated at 37°C and 5% CO₂ for 3 h. After 3 h, remaining media was added, and the incubation was continued, and the media was changed every third day. On day 5, the cell-sample construct was moved to the new well and washed twice with 1X PBS. The Live/Dead assay solution containing calcein AM and ethidium homodimer (EthD-1) diluted in 1X DPBS was added to the samples and incubated for 30 min at 37°C. The viable cells attached to the samples were indicated by the green fluorescence of calcein which has been enzymatically converted from calcein AM by live cells. Similarly, the dead cells were indicated by the red fluorescence obtained due to the binding of EthD-1 that entered through the ruptured cells to the nucleic acid.

2.2.11 Statistical analysis

All the experiments were carried out in triplicates for each composition and the results were represented as mean \pm SD. Statistical analysis of obtained results was carried out using a one-way analysis of variance (one-way ANOVA). To depict statistically different groups Tukey's test with $p < 0.05$ was carried out.

2.3 Results

2.3.1 Setting Time

The initial and final setting time for smart CaP cements with different concentrations of BT at a constant L/P ratio of 0.35 ml g⁻¹ are presented in Table 2.4. No significant variation ($P > 0.05$) were observed except for 10wt.% BT samples. The CPC-10BT samples displayed significantly ($P < 0.05$) lower final setting time when compared to other formulations.

Table 2.4: Setting time for smart CPCs with various wt.% BT

Cement	Initial Setting Time (min)	Final Setting Time (min)
CPC-0 BT	8.83 \pm 0.72	15.33 \pm 0.24
CPC -10 BT	7.58 \pm 0.12	13.67 \pm 0.62*
CPC -20 BT	7.92 \pm 0.42	15.17 \pm 0.51
CPC -30 BT	8.08 \pm 0.72	16.33 \pm 0.24
CPC -40 BT	8.50 \pm 0.35	15.92 \pm 0.42

* - represents significantly different from rest of the composition.

2.3.2 Mechanical Properties

The results of compressive strength of smart CPC samples with varying wt.% of BT are displayed in Figure 2-1. All compositions showed similar compressive strength without any significant differences ($P > 0.05$). This indicates the negligible effect of BT addition on compressive strength of CPC cements up to 40 wt. %.

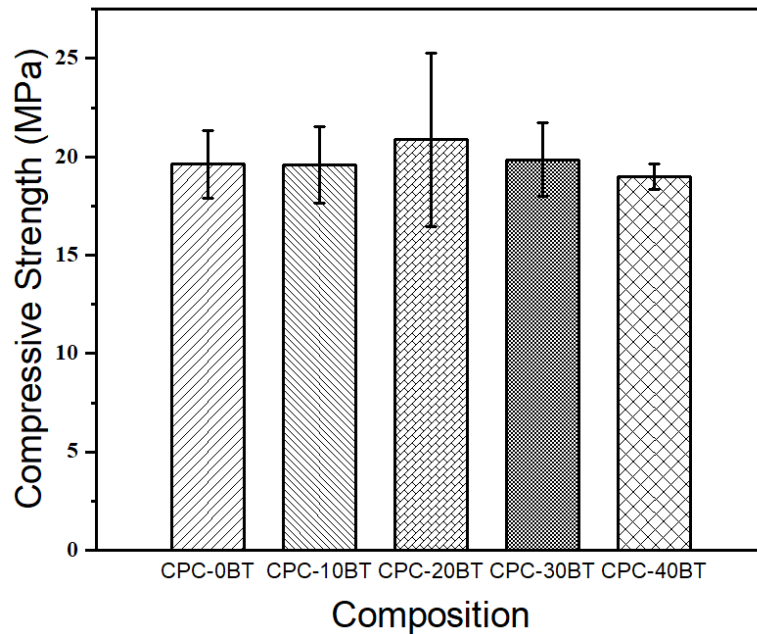


Figure 2-1: Compressive Strengths of different compositions of smart CPCs

2.3.3 Physical characterizations

2.3.3.1 XRD Analysis

The self-setting smart CPC-x BT cement samples were crushed into powder used for XRD analysis. The XRD spectra of the respective specimens are shown in the Figure 2-2. All major peaks of CPC-0BT correspond to monetite (JCPDS PDF# 97-003-8128). With incorporation of BT into PMP, apart from monetite, new peaks corresponding to barium titanate (JCPDS PDF# 97-002-7969) are identified. All the XRD peaks of BT show much

high crystallinity as compared to monetite. The major peak of BT is present at the 2θ angle of 31.5° along the plane [101], and its intensity intensifies with increasing doping %. The XRD analysis also picked up small traces of newberyite ($\text{MgHPO}_4 \cdot 3\text{H}_2\text{O}$) and calcium dihydrogen phosphate ($\text{Ca}(\text{H}_2\text{PO}_4)_2$).

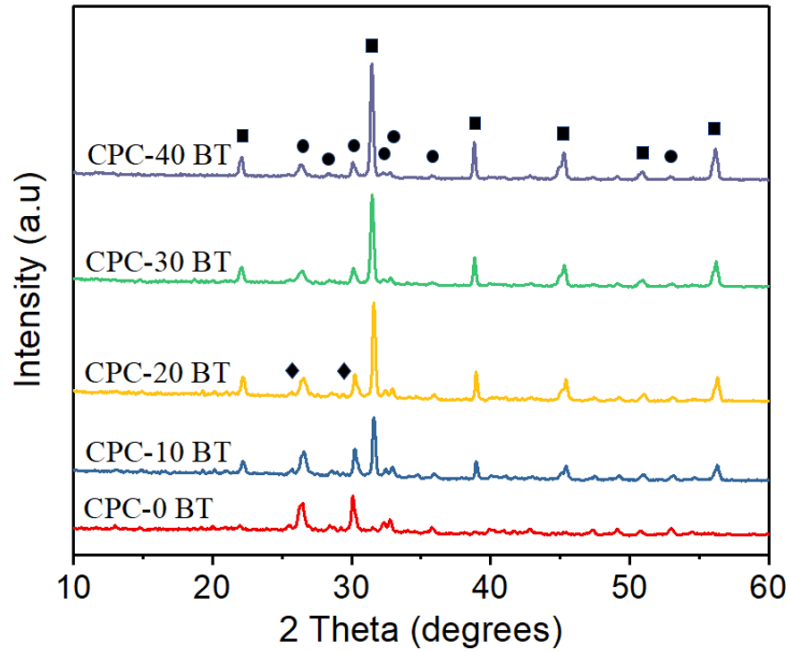


Figure 2-2: XRD patterns of CPC with various wt.% BaTiO_3 (‘■’ represents BT, ‘●’ represents monetite and ‘◆’ represents newberyite)

2.3.3.2 FTIR Analysis

The FTIR spectra of smart CPCs with different concentration of BT are presented in Figure 2-3. All samples have similar absorbance spectra with the presence of hydroxyl (OH^-), phosphate (PO_4^{3-})/ hydrogen phosphate (HPO_4^{2-}) and carbonate (CO_3^{2-}) functional groups. OH^- group are observed in the broad stretching band at $3000\text{-}3500\text{cm}^{-1}$ which corresponds to absorbed water and at 1650 cm^{-1} [69,91]. The CO_3^{2-} band are located near 1415 cm^{-1} like all biological apatite [92]. The band at 1020 cm^{-1} accounts for stretching mode of P-O bond

[64]. The shoulder peaks at 880 and 1060 cm^{-1} can be attributed to the presence of PO_4^{3-} and /or HPO_4^{2-} . The presence of several visible peaks and shoulder in the region of absorbance spectra of the phosphate region (900-1200 cm^{-1}) for all CPC-x BT samples implies the crystallinity of monetite even in the presence of BT [69]. In addition to these functional groups, the stretching band at 790 cm^{-1} corresponding to Si-O-Si (siloxane) group is observed [93].

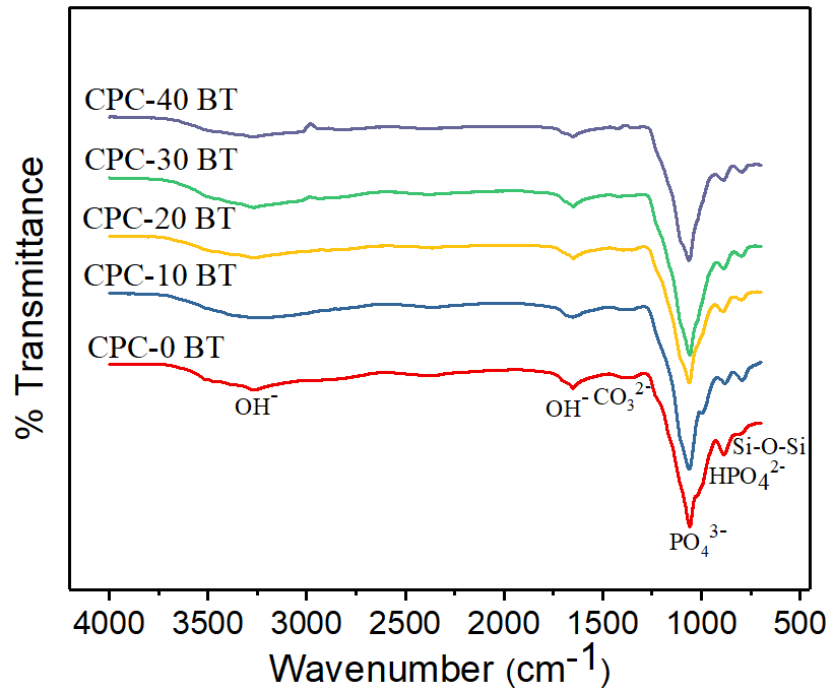


Figure 2-3: FTIR spectra of smart CPC formulation with varying wt.% BT

2.3.3.3 Morphological observation of cements

The SEM images of smart CPC-x BT are shown in the Figure 2-4. All the cement specimens were composed of plate-like DCPA crystals [64,66,67]. Back scattered SEM images projected BT particles (Figure 2-4 (b)-(f)) as white spherical structures distributed homogeneously all over the cement surface area. The surface morphology revealed high crystalline DCPA structures in CPC specimen especially with 10 and 20 wt. % BT

incorporation. Higher magnification image (Figure 2-4(f)) shows the morphology of the BT particles assimilated over the CPC matrix. As expected, with increase in BT wt. % in the sample composition, the concentration of white agglomerates also increased.

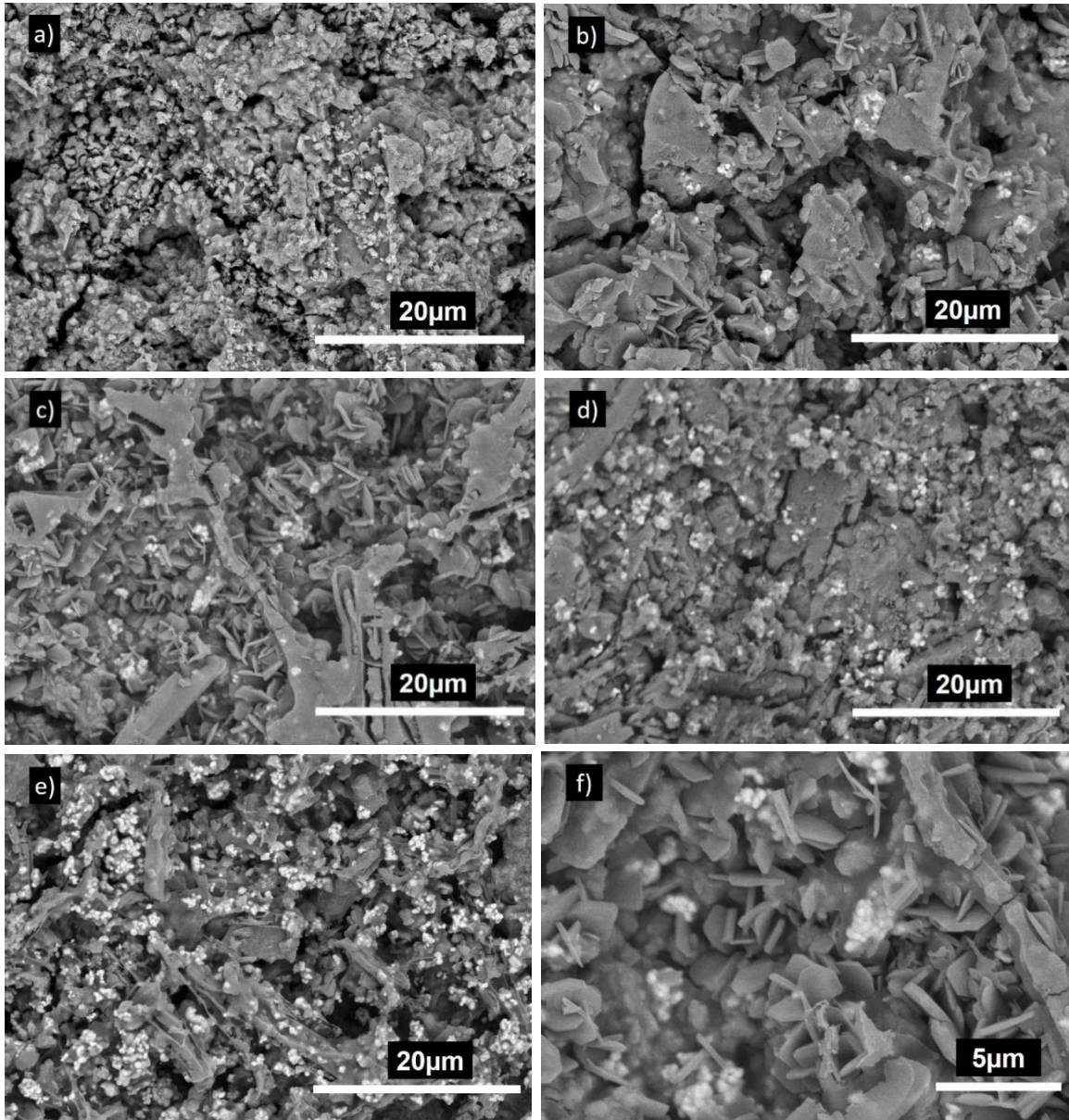


Figure 2-4: SEM images of (a) CPC-0BT (b) CPC-10BT (c, f) CPC-20BT (d) CPC-30BT (e) CPC-40BT

2.3.4 Simulated body fluid (SBF) immersion

The bioactivity of smart CPC with 0,20 and 40 wt. % BT were examined via SBF immersion test. After soaking the samples in $1.5 \times$ t-SBF for 7 days, they were characterized by SEM and the results are shown in Figure 2-5. Uniform dense layer of globular and flower-like structure covered the whole surface of the specimens. With the similarity in morphology they can be identified as apatite. Coatings resulting from SBF immersion usually result in the formation of apatite. Moreover, incorporation of BT did not influence the bioactivity of the samples.

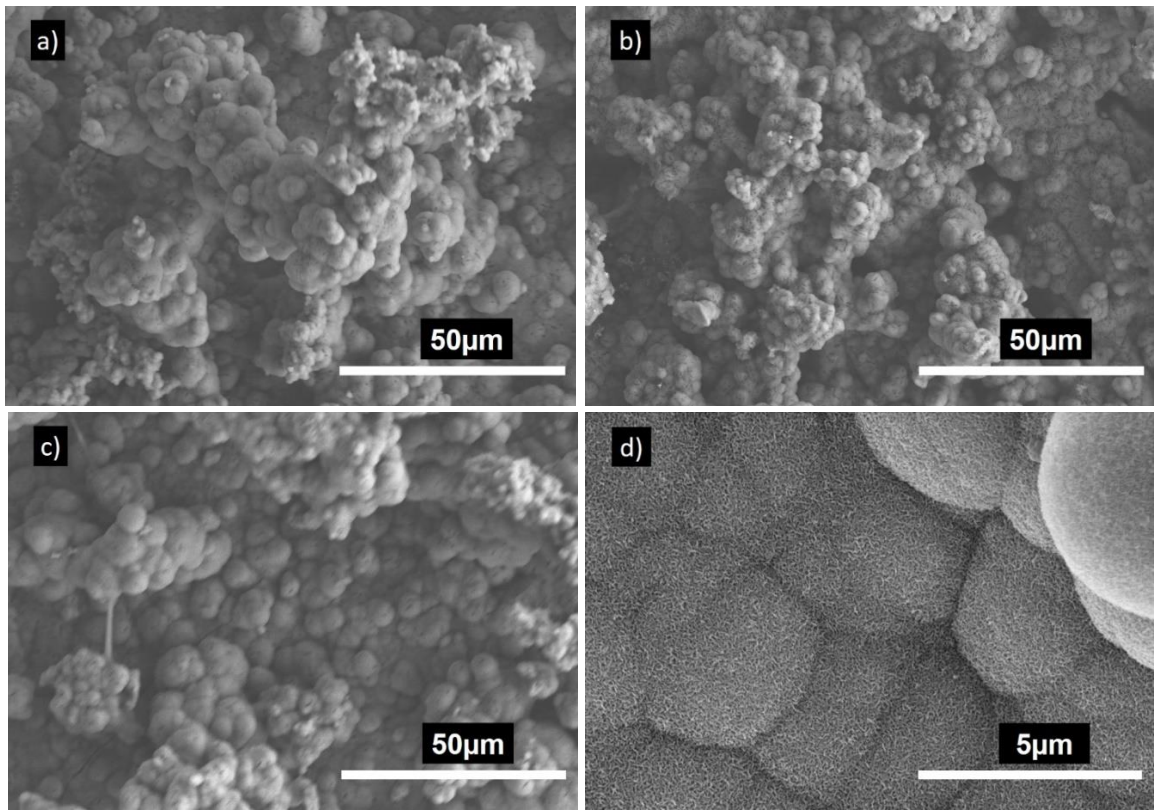


Figure 2-5: SEM images of (a)CPC-0 BT, (b, d) CPC-20 BT and (c) CPC-40 BT after 7 days immersion in $1.5 \times$ SBF

2.3.5 Injectability

All CPC formulations with and without BT showed good injectability without any filter pressing. The injectability of smart CPC-x BT pastes are presented in Figure 2-6. All compositions retained their injectability up to 5-6 min after starting to mix the powders and colloidal silica.

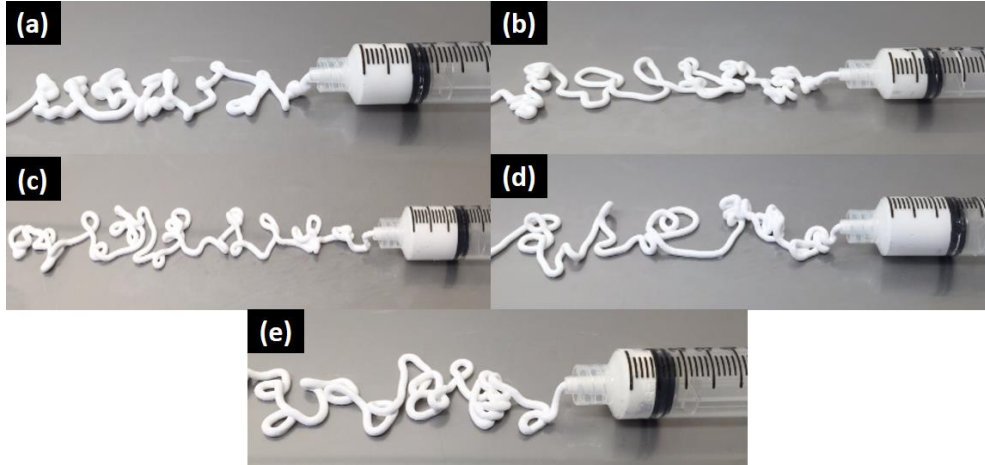


Figure 2-6: Injectability of smart CPC-x BT formulations where (a) $x=0$ wt.% (b) $x=10$ wt.% (c) $x=20$ wt.% (d) $x=30$ wt.% and (e) $x=40$ wt.%

2.3.6 Washout Resistance test:

All CPC formulations injected into SLS solution showed excellent resistance against deterioration in a harsh environment created by SLS. No signs of disintegration were observed after keeping those in SLS for 5 min. The images shown in Figure 2-7 show the absence of any degradation after 5 mins signifying good washout resistance of the cement samples. The samples were continued immersion for 24h and after the specified time frame, no disintegration was observed.

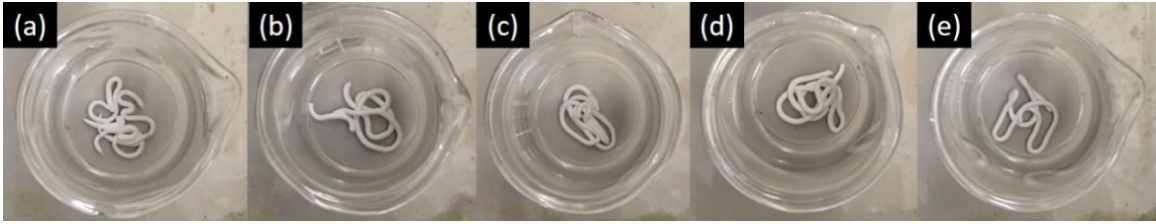


Figure 2-7: Washout resistance test in SLS (a) CPC-0 BT (b) CPC-10 BT (c) CPC-20 BT (d) CPC-30 BT and (e) CPC-40 BT after 5 min

2.3.7 Biodegradation:

Figure 2-8 shows the weight loss evaluation of various cement samples *in vitro*. The medium used for testing was $1.5 \times$ SBF and the results are expressed in terms of weight loss %. For CPC samples with 0 and 20 wt. % BT, weight loss rates are comparable with similar weight loss rate. Although no statistical difference was observed, 40 wt. % samples showed comparatively less degradation rate as compared to 0 and 20 wt. % samples.

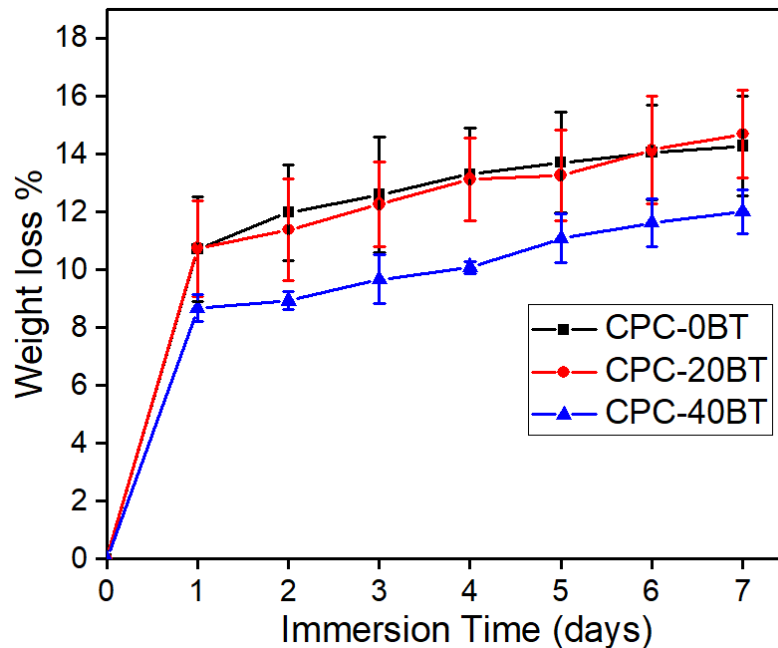


Figure 2-8: Weight loss % of CPC-x BT samples in $1.5 \times$ SBF at different point of time

2.3.8 Cytocompatibility

The *in vitro* cell proliferation tests were carried out on 0,20 and 40 wt.% samples with pre-osteoblast OB-6 cells extracted from mice and the results are presented in Figure 2-9. HA was used as a negative control for the cell studies. The number of cells is proportional to the optical density (OD) readings and thus the results are presented in terms of OD450 readings. After 24h period, the number of cell attached on CPC-20BT samples were observed to be lower ($P<0.05$) as compared to CPC with 0 and 40 wt.% samples. However, there were no significant difference ($P>0.05$) in the number of cells attached when compared with the HA control. On contrary, cell cultured with 40 wt. % samples extracts showed significantly lower ($P<0.05$) values than rest of the CPC formulations and HA control extracts after 72h period. This implies that CPC-40 BT samples exhibited lower cytocompatibility with an increase of incubation time, as compared to CPC-20 BT, which helped in enhanced cell proliferation over 72h.

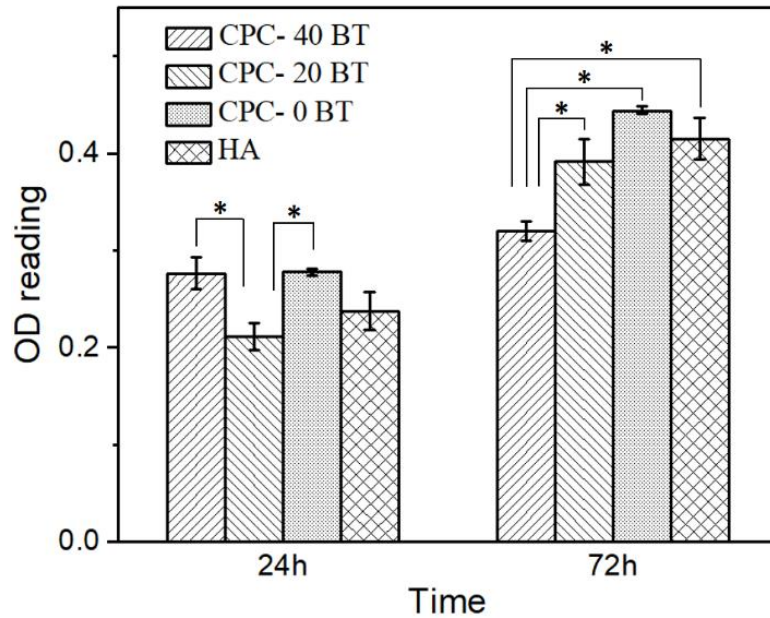


Figure 2-9: O.D. values of OB-6 pre-osteoblast cells seeded in extract of smart CPC-x BT formulations and HA for 24h and 72h, * refers to statistically different pair ($p<0.05$)

The results from live and dead assay are presented in Figure 2-10 where the viable and dead cells represented by green and red fluorescence respectively. The CPC-0BT showed relatively lower number of cells attachment and proliferation than smart CPC formulations with BT. Moreover, CPC- 20/40 and HA control comparable number of live cells attached to their surfaces implying higher cell proliferation on BT incorporated samples.

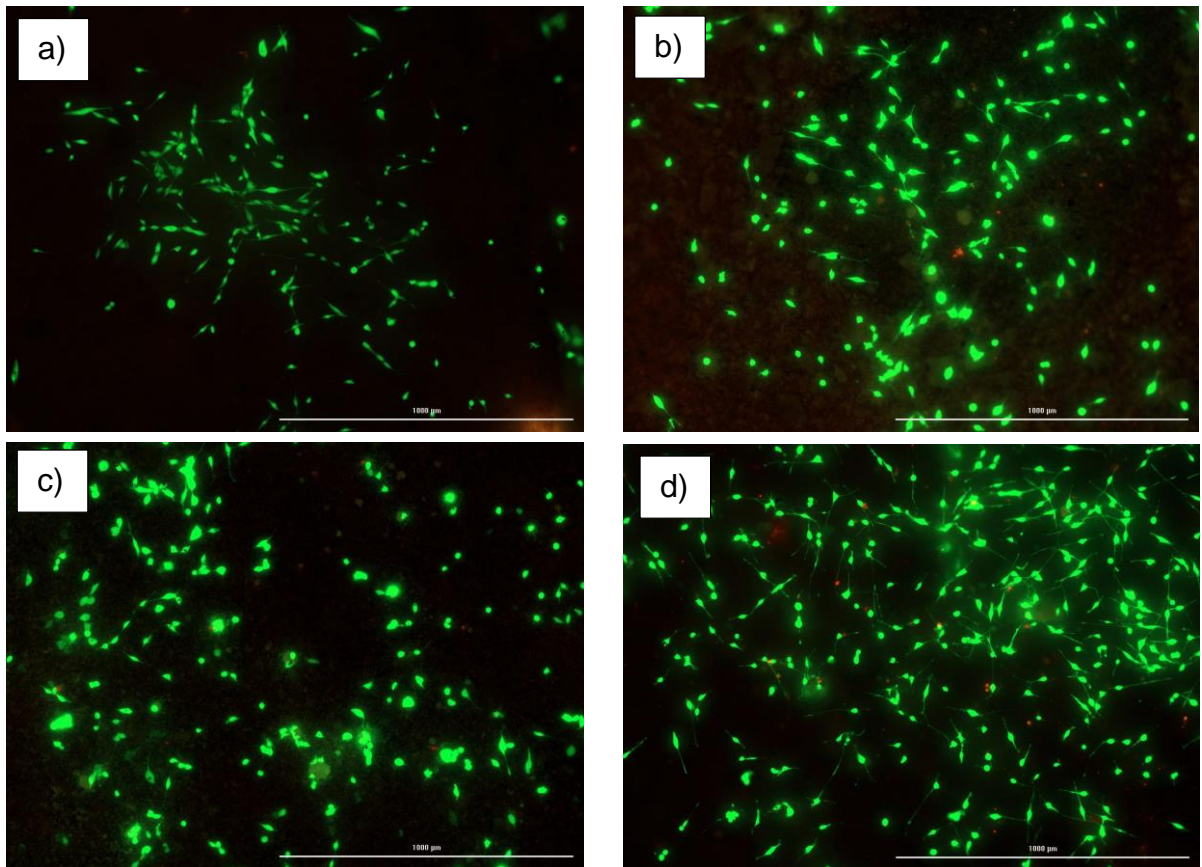
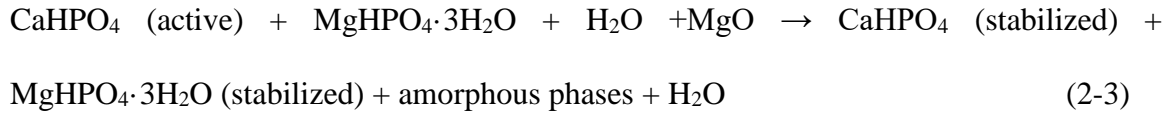
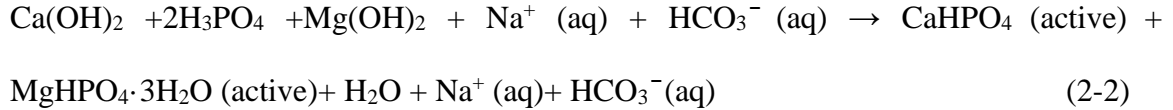


Figure 2-10: Live and dead cell assay for the cells attached and proliferating along the surface of a) CPC-0 BT, b) CPC-20 BT, c) CPC-40 BT, and d) HA surface at day 5. The viable cells are indicated by the green fluorescence and dead cells by the red fluorescence. Scale 1000 μm .

2.4 Discussion

Magnesium ion (Mg^{2+}) is the second most abundant intracellular divalent cation and has been known for its involvement in diverse cellular functions. Since Mg^{2+} assists in bone mineral metabolism, formation and crystallization process, in addition to the Ca^{2+} ion the PMP has been integrated with magnesium hydroxide [$Mg(OH)_2$] [94-96]. At the beginning of our study, setting time was measured by using PMP, MgO as powder phase and colloidal silica as a liquid phase. This composition completely set within 3 min and did not allow sufficient working time as the ideal handling requirements for an injectable CPC are: initial setting time 3-8min, cohesion time ≥ 1 min and final setting time ≤ 15 min [4,5]. The setting time can be modified by adjusting the cement composition and incorporating additives such as sodium orthophosphates, citric acid, gelatinized starch [5], borax or sodium borate decahydrate ($Na_2B_4O_7 \cdot 10H_2O$) [97], p-chitosan [66], surface-modified multi-walled carbon nanotubes [67], and colloidal silica [69]. The present study uses borax as a setting time retardant. After numerous trials, the optimal concentration of borax was identified to be 4 wt.% as this resulted in initial and final setting time approximately 8min and 15 min respectively (Table 2.4).

The setting mechanism of CPC is a continuous process and can be dissociated into two parts. First, the interaction between Ca^{2+} and Mg^{2+} with excess $H_2PO_4^-$ and HPO_4^{2-} , forms a network to provide initial stability, and is responsible for initial cement setting [69]. The second part involves the hardening mechanism via entanglement of the precipitated crystals and thus results in final setting [4,5]. The relevant chemical reactions involved during setting can be summarized as:



Generally, the infusion of BT within the cement samples lowers the overall concentration of active self-setting CaHPO₄, accounting for reduced matrix entanglement which in turn increases setting time. In addition, BT addition undermines the physical bond between plate-like monetite crystals resulting in reduced mechanical strength. Except 10 wt. % BT samples, all the samples have trivial differences (p>0.05) in the setting time values. Significant reduction of setting parameters for 10 wt.% samples can be attributed to higher siloxane group formation (Figure 2-3) in these samples as indicated in our FTIR results. The self-hardening CPCs must exhibit a mechanical strength at least equivalent to trabecular bones i.e., 10MPa [5]. All as- prepared CPCs displayed strength higher than 15MPa proving their viability in orthopedic applications (Figure 2-1). No detrimental effect on compressive strength occurs up to 40 wt.% of BT addition. Up to 10.0 vol.% (or 35 wt.%) BT content filled within PMMA bone cements, R.G. Carrodeguas et al. [70] reported insignificant effect on ultimate compressive strength of cement. The subunits of colloidal silica particles are usually un-joined Si(OH)₂. Initially OH⁻ at the surface of colloidal silica particles assists in electrostatic dispersion of cement reactants among nanosilica particles [69,93]. The colloidal silica particles then interact together and polymerize into a 3D network of siloxane (Si-O-Si) groups forming a bond between as-produced DCPA, newberyite crystals and incorporated BT simultaneously [93]. Therefore,

colloidal silica condensation to siloxane via gelling mechanism [93] defied setting time increment and compressive strength decrement in our cement samples.

The prime constituent of PMP being $\text{Ca}(\text{OH})_2$ and H_3PO_4 , the XRD analysis (Figure 2-2) shows major peaks for monetite. Also, due to the presence of $\text{Mg}(\text{OH})_2$ as a precursor, newberyite peak was observed in XRD results. Mg^{2+} and Ca^{2+} cations have similar chemical affinity; thus, formation of newberyite is anticipated. Additional BT peaks in BT incorporated samples without any changes in the phases and crystal structure implies no undergoing chemical reaction involving BT in samples. Our reaction system has a molar ratio of $(\text{Ca} + 0.5\text{Na})/\text{P}$ less than 1 (i.e. excess phosphoric acid), and consist of Ca^{2+} , Mg^{2+} and Na^+ cations. Yet, XRD results did not show peak of other phases such as $\text{Ca}(\text{H}_2\text{PO}_4)_2$, $\text{Mg}(\text{H}_2\text{PO}_4)_2$, NaH_2PO_4 . Since microwave synthesis favors amorphous phases, other abovementioned phases might have formed amorphous compounds by partial transformation of H_2PO_4^- and HPO_4^{2-} ions with the available cations [44,68]. The SEM images (Figure 2-4) revealed the presence of large plate-like monetite crystals. The distribution of plate like crystals can be seen throughout the surface of 10 and 20 wt. % BT samples. The plate-like monetite crystals have a capability of forming a network easily by interacting with each other. This network accelerates the initial stabilization of cement and reduces the solidification time. Thus, although insignificant but the 10-20 wt. % of BT addition led towards the lower initial setting time. Furthermore, the surface morphology at higher magnification (Figure 2-4(f)) confirmed the infusion of BT within CPC structure. Incorporation of ferroelectric BT contributes towards the enhancement of electrical properties of formulation simulating the actual bone scenario. Under stress condition, BT generates electrical charges on the sample surfaces. Negative charges on sample surface

adsorbs Ca^{2+} cations which acts as nuclei for the formation of Ca-P layer [30]. Ca^+ cations also facilitates the protein adhesion such as integrins, fibronectin and osteonectin. On the other hand, limited apatite formation is expected from positive charges on the surface as they attract antiadhesive anionic groups such as HPO_4^{2-} and HCO_3^{2-} [98]. The colloidal silica is also responsible for the apatite nucleation and growth [99]. Even though the increment of apatite on SBF immersed BT incorporated samples were insignificant, these samples under *in vivo* stress condition are expected to increase the apatite formation as compared to CPC-0BT.

As we are dealing with injectable cement, the more realistic evaluation of washout resistance will be injecting cement paste into SLS right after loading into the syringe and the test were carried out following this approach. Magnesia, MgO, enhances the anti-washout property of Calcium phosphate cements. Moreover, the binding property of silica with CPCs and BT is also expected to improve the washout resistance. The washout resistance of monetite cement with and without chitosan in SLS as reported by Touny et al. [64] were 1h and immediate dissociation into powder respectively. Our cement formulations have better washout resistance as all formulation maintained their shape even after 24h.

Bone graft cements demands for combination of good injectability and proper hardness to minimize invasiveness of surgery [5]. It is noteworthy that the as-prepared CPCs formulations maintained proper injectability up to 5-6 min along with high workability and cohesion time. When compare to the commercially available Norian SRS[®] cements, present CPC formulation displayed superiority in terms of injectability. Norian SRS[®] cements exhibit filter pressing with 1.5mL uninjectable cement out of 4.5mL [5]. Whereas

with 5mL of our formulation paste inside the syringe, each of our composition avoided this phenomenon. More often addition of fillers in CPCs reduces porosity causing slower resorption, slow bone substitution, poor injectability and other rheological properties [5]. On contrary, in our work the addition of BT as filler will be promoting bone substitution rate, while injectability and degradation rate remained unaffected. R.G. Carrodeguas et al. [85] reported acceptable setting parameters, compressive strength, radiopacity, and injectability for surgical procedures with 20-50 wt. % of untreated or silanated BaTiO₃ or SrTiO₃ in acrylic bone cements. The addition of 20-40 wt.% BT into our CaP structure is expected to provide sufficient the radiopacity to the cement under fluoroscopy. While considering the biodegradability aspect, BT ≤ 20 wt. % in cement samples are more favorable.

In vitro cytocompatibility tests are crucial preliminary tests for biomaterials before moving forward to more complex and expensive *in vivo* experiments. The WST-1 assay OD reading after 24h revealed lowered number of cell attachment on 20 wt.% samples than 0 and 40 wt.% sample, however, they were comparable to HA control. The biocompatibility behavior of particulate filled composite can be different from its identical bulk composite [29]. This can be the plausible reason behind the low OD reading of 20 wt.% samples as compared with 0 wt.% samples. As a surprise, the initially inhibiting 20 wt.% samples showed OD reading comparable($p>0.05$) to 0 wt.% samples and HA control after 72 h period. Fine (<2 μ m) wear particles can translocate to the different organs via systemic circulation and lead to cell toxicity [29]. BT used in this study had a particles size of less than 2 μ m. Therefore, the reduced OD values for 40wt.% samples after 72h period can be due to the presence of excessive fine BT particles. This clearly indicates CPC-20 BT to be

the optimum composition for biocompatible ferroelectric CPC cement. All the samples showed higher OD reading as compared to 24h period implying the cell proliferation on CPC-x BT samples. Furthermore, the live and dead cell assay after 5 days incubation clarified the non-toxic nature of cement samples incorporated with BT. Higher cell proliferation on CPC-20/40 BT sample as compared to CPC-0BT thus implies the enhancement of earlier stage osteogenesis.

2.5 Conclusion

Smart CaP cements incorporated with ferroelectric BT were synthesized using microwave energy and colloidal silica. The as-prepared CPCs were bioactive, biocompatible, and most importantly bio-degradable. Upon stress conditions, the samples are expected to exhibit higher bioactivity, cell proliferation, and thus results in higher bone formation. All cement formulation behaved in a similar fashion regarding setting time, mechanical strength, bioactivity, injectability and washout resistance. Moreover, based on the cytocompatibility and biodegradation rate, we conclude the most favorable CPC composition for better cell viability and biodegradation to be 20 wt. % of BT. These promising physical, mechanical and biological characteristics of novel injectable piezoelectric CPCs makes them a possible candidate for a new generation smart biodegradable CaP bone cement.

Chapter 3

3. Conventionally sintered hydroxyapatite-barium titanate piezobiocomposites

3.1 Introduction

Annually, five to ten percent of 6 million fractures can be classified as bone union issues in the United States. The treatment cost accounts for another \$3billion-\$6 billion of the economic expenses [100]. Most often, long bone fractures results in complications namely, delayed union, nonunion, and false union or occurrence of pathology [70,100]. The bone inherent electrical properties are integral in bone development healing/ remodeling process and has been the source of inspiration for different researches [12-14]. To overcome these bone union issues, electrical stimulation has been applied to enhance the neo-bone formation rate [16-19,100]. Moreover, recent studies focus on the development of self-powered piezoelectric devices and piezoelectric ceramics for different orthopedic and spinal applications [12-14,20,21,25-27,29,30,42,101]. Hydroxyapatite (HA) with its similarity to the chemical composition of bone, teeth and hard tissues mineral makes it a perfect candidate for bone substitutes [33,34,43]. It is renowned for high biocompatibility, osteoconductivity, non-toxic, non-inflammatory, non-immunogenic and bioactive nature [35]. Incorporating piezoelectric material with HA has been quiet an intriguing research topic for hard tissue engineering and is the prime focus of this chapter.

There have been enough evidences in the literature which states the incorporation of BT into HA. Piezoelectric nature of BT has been utilized in *in vivo* [21,25,27,29,101] and *in vitro* [13,26,30] experiments for the improvement of interfacial strength, cellular activities, tissue ingrowth, and neo-bone formation. A study on jawbones of dogs by Jianqing et al. claimed earlier osteogenesis on polarized HABT implanted as compared to the bulk HA counterpart [21]. On contrary, Park et al. observed no substantial difference between the polarized and nonpolarized dense BT specimens *in vivo* [27]. The *in vivo* experiment on rat conducted by Nacer et al. [101] with castor bean polymer doped with SiO₂ or BT reported higher osteogenesis and neo-bone formation on BT doped group. Furthermore, Ciofani et al. [102,103] reported the high concentration (100µg/ml) cytocompatibility of BT nanoparticles (BTNPs) when dispersed in glycol-chitosan and Doxorubicin. Not so far off, Ball et al. [104] reported the comparable short-term biocompatibility of porous BT foamed ceramics to porous 45S5 Bioglass®.

Porous HA improves rapid bone ingrowth whereas dense HA is a necessity in load-bearing applications [105]. Accordingly, studies on dense bioceramics product characterization can be a key step towards proving their viability in biomedical applications and sintering technique has been widely implemented for the fabrication of such dense HA products. Among different sintering techniques, currently, spark plasma sintering (SPS) has been the most popular one. This technique promotes densification and decreases sintering temperature and/or time [3]. From a commercial perspective, SPS is capital intensive and requires expertise, thus it might not be industrially viable. On the other hand, conventional pressureless sintering is easy to fabricate, economic and also industrially viable. In addition, although SPS can result in mechanically and electrically better composites than

pressureless conventional sintering, often this inferiority can lie in the acceptable range for orthopedic applications [3,41]. Therefore, this chapter aims in fabricating and characterizing HA-BT composites by conventional sintering. Efforts have been employed to study the differences in the properties of the sintered HA-BT composites in the present case, to the SPS-ed specimens present in the literature.

3.2 Experiments

3.2.1 Materials and sample preparation

Fisher laboratory educational grade HA used for the preparation of samples. Barium titanate (IV) (BaTiO_3 , 99.5%, particle size $\leq 2\mu\text{m}$) and Polyvinyl alcohol (PVA) (87-90%) were purchased from Sigma-Aldrich. Initially all powders were homogeneously mixed manually using a mortar and pestle. For each 5gm of HA+BT composition, 0.05g of PVA was added as a binder. Samples comprising 0,20 and 40 wt.% BT were prepared and are represented as HA-x BT. The detail chemical compositions are listed in Table 3.1. To prepare a sample pellet, 1g of mixed powder was inserted in a die of $\frac{1}{2}$ inch diameter and uniaxially pressed at approximately 65-70MPa for 3 min. These compacted pellets were then subjected to conventional ramp and hold sintering technique inside a conventional sintering furnace (Zircar Zirconia, Inc., Florida, NY). The pellets were subjected to heating cycle consisting of two steps: firstly, sample pellets were heated from room temperature to 1200°C at a heating rate of $10^{\circ}\text{C}/\text{min}$ followed by temperature hold at 1200°C for 1h. The samples were then allowed to cool down to room temperature at furnace cooling rate. These cooled samples were then subjected to different tests.

Table 3.1: Various compositions of sintering samples

Composition	HA (g)	BT (g)	PVA (g)
HA	5.00	-	0.05
HA-20BT	4.00	1.00	0.05
HA-40BT	3.00	2.00	0.05

3.2.2 Physical Properties

Bulk density and apparent porosity were used to evaluate the physical properties of all sintered samples. The bulk density was calculated with mass and geometrical volume of sintered samples. To obtain the apparent porosity of samples, initially the dry weight of the sample ' W_d ' was measured. Then the sample was immersed in the DI water and ultrasonicated for 15 min. The sample was kept immersed overnight. The sample was then taken out and soaked weight ' W_s ' was measured. The apparent porosity was calculated using following equations:

$$\text{Sample volume} = \frac{\pi D^2}{4} \times t$$

Where 'D' and 't' are diameter and thickness of the corresponding sample.

$$\text{Apparent porosity} = W_s - W_d = \text{Water absorbed by sample}$$

$$\text{Volume of soaked water} = \frac{\text{Water absorbed}}{\text{Density of water}}$$

$$\text{Apparent porosity}(\%) = \frac{\text{Vol. of soaked water}}{\text{Sample vol.}} \times 100$$

3.2.3 Mechanical Properties

3.2.3.1 Compressive strength

The dimensions of as-prepared sintered samples were measured using Vernier caliper before performing mechanical properties. The uniaxial compression test was carried out on samples using a universal testing machine with 50 KN load cell (model 5569, Instron, Norwood, MA, USA). As per the protocol of the American dental association i.e. $0.75 \pm 0.25 \text{ mm min}^{-1}$, the crosshead loading rate of 0.5 mm min^{-1} was set [66]. The compressive strength (σ_{max}) of sample was calculated using following equations:

$$\sigma_{max} = \frac{P_{max}}{A} \text{ and } A = \frac{\pi D^2}{4}$$

Where, P_{max} is peak load during the test, A, and D are cross sectional area and diameter of sample respectively. The test was conducted on triplicates for each composition.

3.2.3.2 Hardness and fracture toughness

The hardness of HA-x BT sintered samples was evaluated through Vickers micro-indentation method at a load of 0.1kg with a dwell time of 10s. All the samples were mounted in an epoxy resin and polished before the test. For each sample ten indentations were made, and the average value is reported as mean \pm sd. The Vickers hardness (HV) values were calculated using standard equation:

$$HV = 0.001854 \times \frac{P}{d^2}$$

Where, P is indentation load, and d is the average diagonal length of indentation. The indentation diagonals and crack length were measured under SEM.

The semi-empirical formula developed by Evans and Charles [106] was implemented for the measurement of sample indentation fracture toughness. With the measurement of

indentation half diagonal ‘a’, crack length ‘c’ and hardness ‘H’, the fracture toughness was calculated as:

$$K_{Ic} = 0.16 H a^{1/2} \left(\frac{c}{a}\right)^{-3/2}$$

3.2.4 Physical characterizations

3.2.4.1 X-ray Diffraction analysis

The phase composition analysis of as-prepared sintered HA-x BT samples were carried out with X-ray diffraction (XRD, Ultima III; Rigaku, The Woodlands, TX) with monochromated Cu K α radiation (44KV, 40mA) over a 2 θ range of 10-60° with a continuous scan mode at a speed of 0.75° min⁻¹. All the phases within the sample were determined using the JADE (MDI, Livermore, CA, USA) software.

3.2.4.2 Fourier transform infrared spectroscopy analysis

Fourier transform infrared spectroscopy (FTIR, UMA-600 Microscope, Varian Excalibur Series, Digilab, Holliston, MA, USA) was performed on each composition to detect the functional groups present within the sintered samples using an ATR diamond crystal. 256 scans within the range of 4000 to 700 cm⁻¹ were performed on each sample.

3.2.4.3 Morphology of samples

Scanning electron microscope (SEM, S-4800, Hitachi, Japan) was employed to examine the surface morphology of as-prepared sintered samples. The samples were mounted on conducting tape and sputter coated before inserting into the SEM vacuum chamber. The grain size of the as-prepared samples was evaluated from SEM micrographs using image J

software (developed at the National Institutes of Health). The grain size of more than 100 grains were measured and the average value has been reported.

3.2.5 Bioactivity of samples in simulated body fluid(SBF)

To assess the bioactivity of sintered samples, each sample was immersed in 50ml of $1.5 \times t$ -SBF at 37°C for 7 days with the SBF being replenished every 48h. The $1.5 \times t$ -SBF [86] was prepared by dissolving reagent grade NaCl, NaHCO_3 , KCl, Na_2HPO_4 , $\text{MgCl}_2 \cdot 6\text{H}_2\text{O}$, 1M HCl, $\text{CaCl}_2 \cdot 2\text{H}_2\text{O}$, Na_2SO_4 and Tris-buffer. At the end of immersion period, samples were rinsed in DI water and air dried.

3.2.6 In vitro cytocompatibility

All composition of sintered CaP samples was prepared, autoclaved and immersed in minimum essential medium-Alpha (MEM- α Thermo Scientific, Logan, UT, USA) with extraction ratio of $300\text{mm}^2/\text{ml}$, and was kept at 37°C and 5% CO_2 for different point of time. MC3T3-E1 osteoblastic cells were also initially seeded in 24-well plate (5×10^4 cells per well) at same 37°C and 5% CO_2 condition for 24h. The conditioned medium collected after 24h was then used to culture the as-prepared MC3T3-E1 cells. After incubating the cells at 37°C and 5% CO_2 for another 24h, cells were treated with thiazolyl blue tetrazolium bromide (MTT, Sigma-Aldrich, St. Louis, MO, USA) for 4 hours, insoluble formazan dissolved in DMSO, and the optical density measured at 570nm wavelength. Non-sintered HA was used as a control. Same procedure was repeated but this time with a conditioned medium collected after 7 days to culture the cells followed by MTT assay after another 24h to evaluate the cell viability.

3.3 Results

3.3.1 Physical and mechanical Properties

Figure 3-1 represents the physical appearance of sintered HA-x BT samples. The indentation made by Vickers microhardness tester and the cracks initiated at the corners are shown in the SEM micrograph in Figure 3-2. The bulk density, apparent porosity %, average grain size, compressive strength, Vickers microhardness, and fracture toughness of as-prepared samples are shown in the Table 3.2. Here, decrease in hardness, and toughness are observed with BT incorporation. On the other hand, porosity increased with addition of BT into HA matrix. Furthermore, the compressive strength remained statistically indifferent even with the addition of BT.



Figure 3-1: HA-x BT sintered samples at 1200°C for 1h

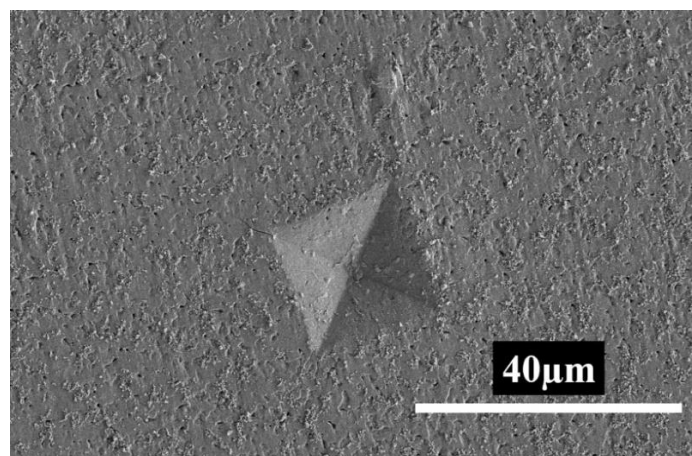


Figure 3-2: Cracks initiated from the corners of HA-20BT Vickers indent

Table 3.2: Physical and mechanical properties of HA-x BT samples

Composition	Avg. Grain size (μm)	Compressive Strength (MPa)	Hardness (GPa)	Toughness ($\text{MPa m}^{1/2}$)	Bulk density (g/cc)	Apparent porosity (%)
HA	0.79 ± 0.31	305.68 ± 23.93	3.55 ± 0.19	0.90 ± 0.05	2.66 ± 0.02	10.46 ± 0.53
HA-20BT	1.75 ± 0.61	345.46 ± 13.67	$2.33 \pm 0.15^*$	$0.85 \pm 0.04^*$	$2.48 \pm 0.07^*$	$22.67 \pm 1.75^*$
HA-40BT	1.95 ± 0.88	350.41 ± 15.28	$1.91 \pm 0.08^{*,**}$	$0.80 \pm 0.04^{*,**}$	2.55 ± 0.04	$25.26 \pm 0.24^*$

* - statistically different with HA ($p < 0.05$), ** - statistically different with HA-20 BT ($p < 0.05$)

3.3.2 Physical characterizations

3.3.2.1 XRD analysis

The XRD pattern of HA-x BT sintered samples are presented in Figure 3-3. HA disintegrated into α and β - tricalcium phosphate (TCP) phases with the incorporation of Barium Titanate into the samples. Also, the dissociation of BT resulted in the formation of Calcium Titanate, Tribarium phosphate and Dibarium titanate and their intensity increased with the increase in BT wt. %. The diffraction peaks for HA (JCPDS PDF# 98-000-0251), β -TCP (JCPDS PDF# 97-009-7500), α -TCP (JCPDS PDF# 97-000-0923), BT (JCPDS PDF# 97-002-7969), CaTiO_3 (JCPDS PDF# 98-000-0350), Ba_2TiO_4 (JCPDS PDF# 97-002-9389), $\text{Ba}_3(\text{PO}_4)_2$ (JCPDS PDF# 97-006-9450) are identified during the analysis.

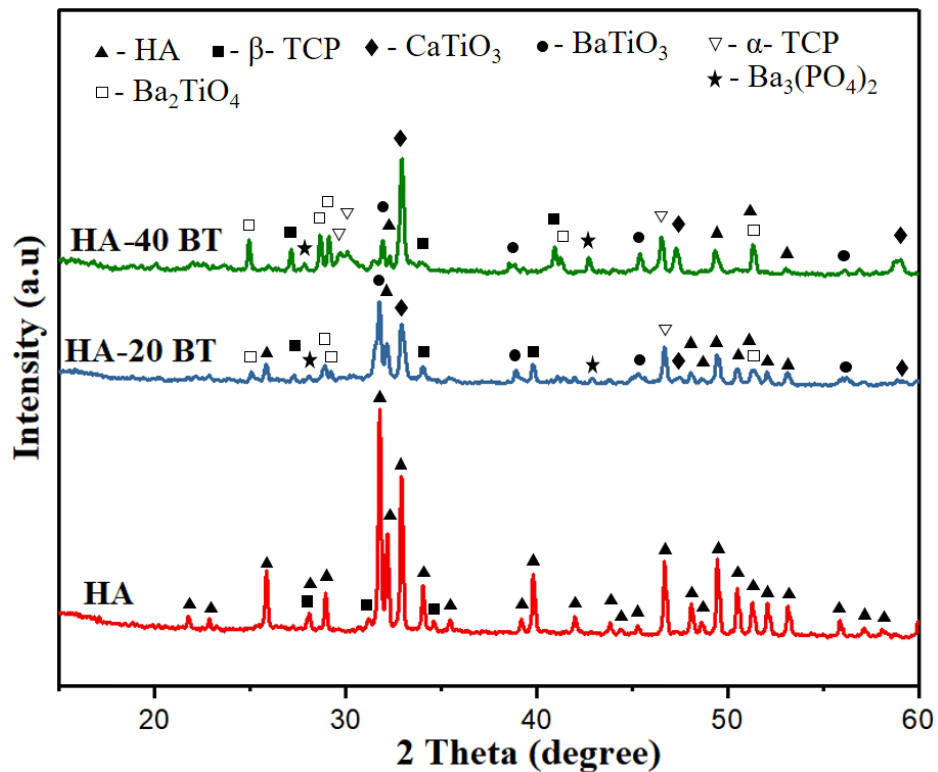


Figure 3-3: XRD analysis of sintered HA-x BT samples

3.3.2.2 FTIR analysis

Figure 3-4 represents the FTIR spectra of HA-x BT sintered samples. Stretching band corresponding to adsorbed water is observed at 3000-3500 cm^{-1} [69,91]. An intense peak seen at 3571 cm^{-1} is due to the stretching vibration of OH^- functional group. The carbonate ν_3 group is identified by peak at 1650 cm^{-1} [107]. Furthermore, the peak for phosphate ν_1 functional group is observed at 961 cm^{-1} and the presence of several peaks and shoulder in the range of 900-1200 cm^{-1} correspond to the phosphate group [69,107]. The presence of BT can be identified by strong and wide band between 495 cm^{-1} to 850 cm^{-1} [83] and the peak trending at the start (700 cm^{-1}) of the FTIR spectra of HA-20/40 BT samples implies the presence of Ti-O group within these samples.

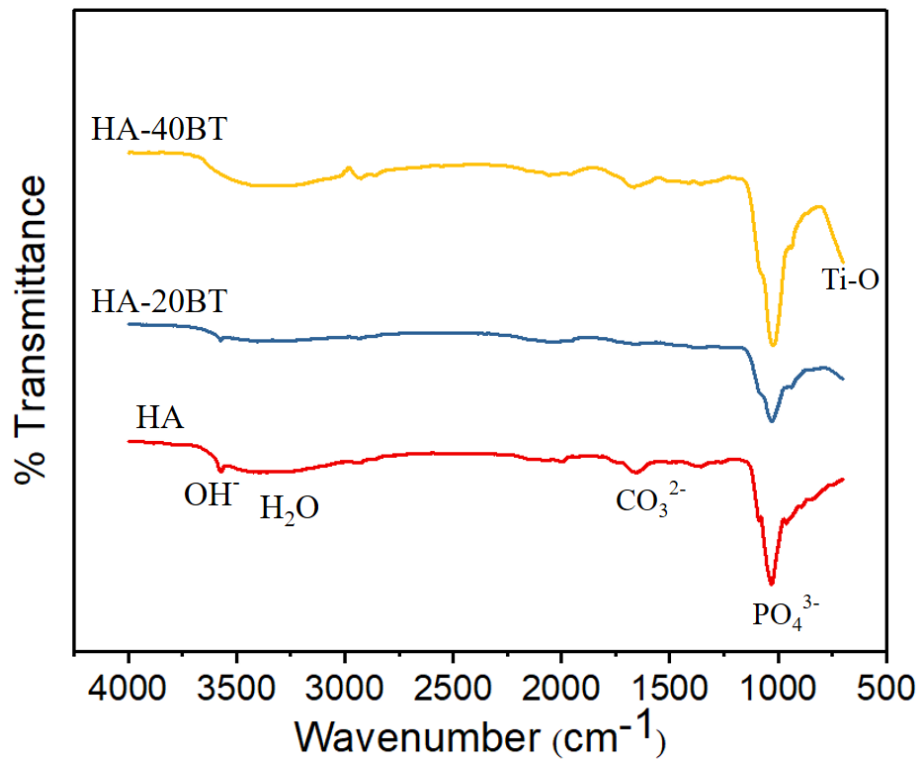


Figure 3-4: FTIR absorbance spectrum of sintered HA-x BT samples

3.3.2.3 Surface Morphology of sintered samples

The surface microstructure of as-prepared HA-x BT sintered samples are presented in Figure 3-5. Smaller grains with average grain size of $0.78\mu\text{m}$ were observed on sintered HA samples. However, the grain size distribution range increased with the increase in the BT wt.%. In addition, the SEM micrograph showed higher number of blowout holes on the surface of HA samples when compare to the BT incorporated samples.

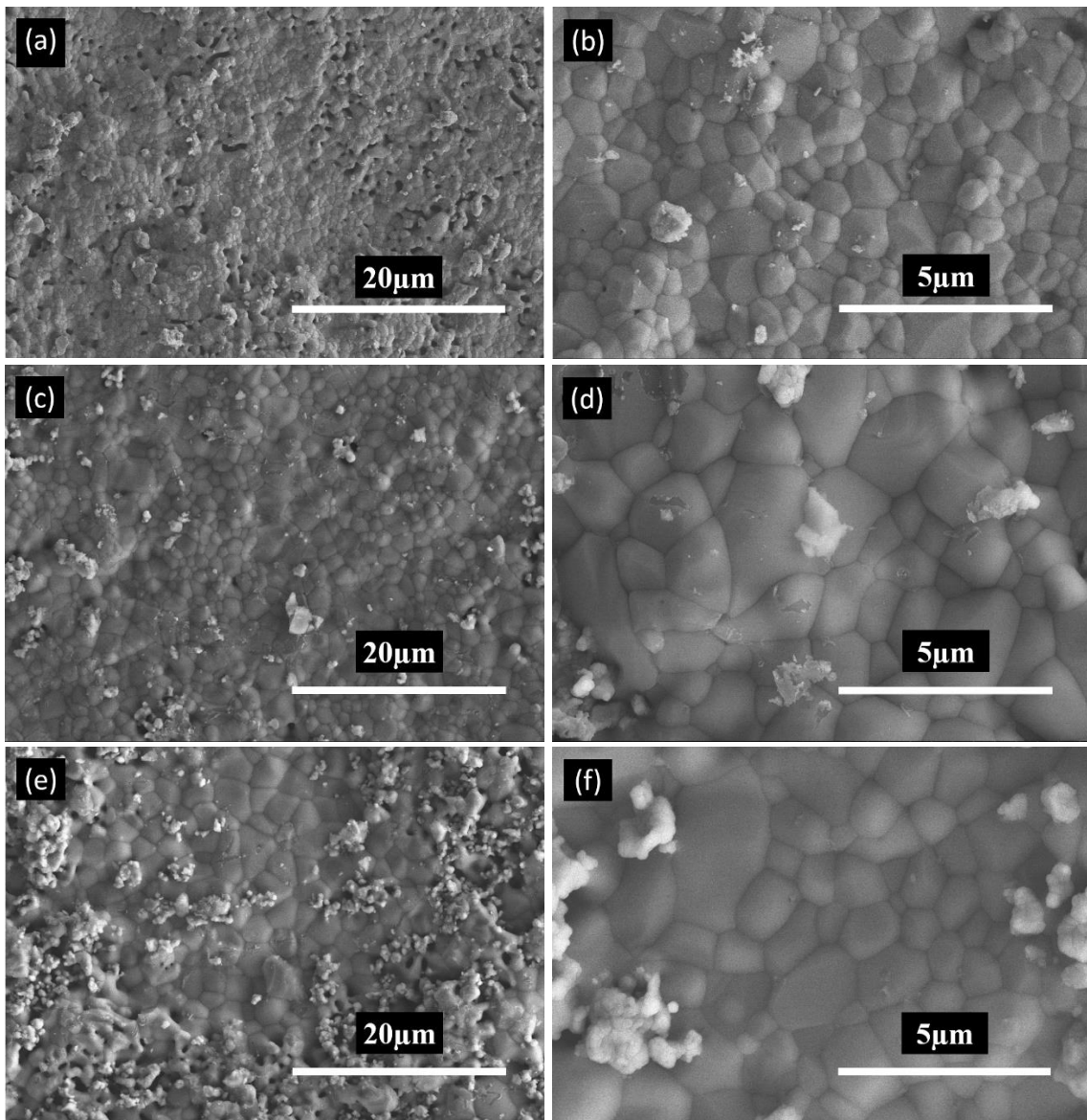


Figure 3-5: SEM images of sintered (a,b) HA (c,d) HA-20 BT (d,e) HA-40 BT

3.3.3 Bioactivity of sintered samples

After 7 days immersion of HA-x BT samples in $1.5 \times t$ -SBF, the surface morphology of immersed samples was analyzed under SEM. All the SBF immersed samples possessed globules and flower-like apatite structure (Figure 3-6(a-c)) implying the good bioactivity of sintered samples. The high magnification SEM image (Figure 3-6(d)) shows the typical morphological feature of apatite.

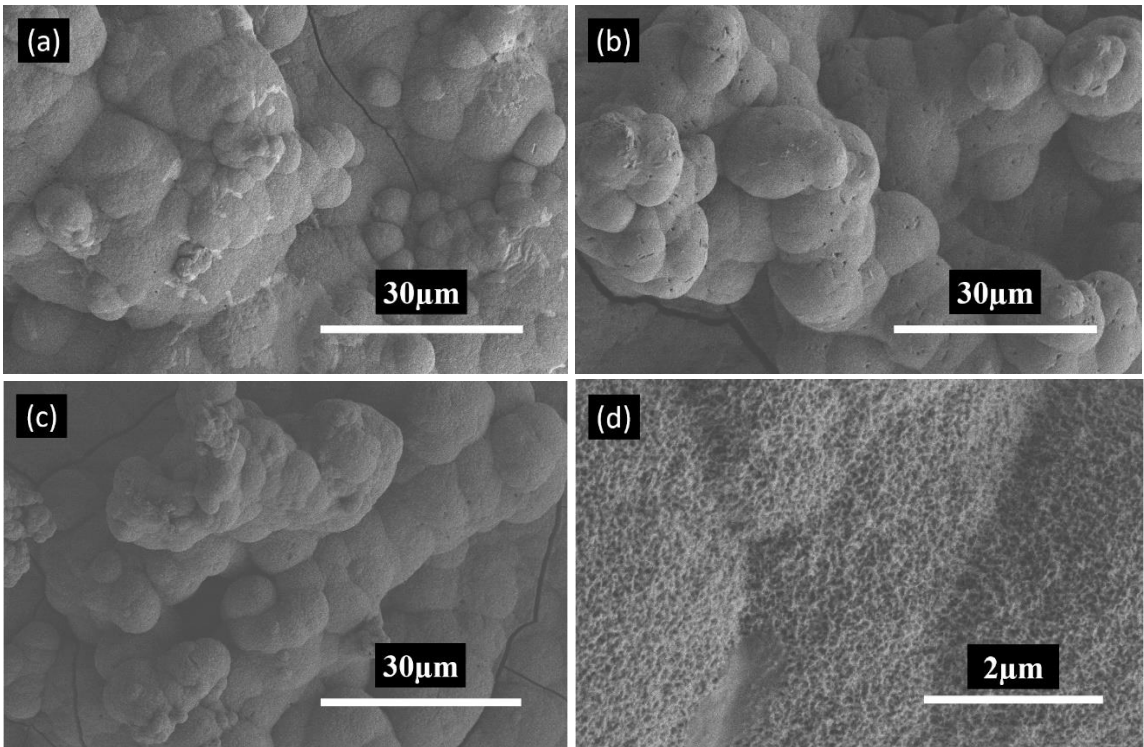


Figure 3-6: SEM images of sintered (a) HA (b) HA-20 BT (c,d) HA-40 BT after 7 days immersion in $1.5 \times t$ -SBF

3.3.4 *In vitro* cytocompatibility

The *in vitro* cell viability results are shown in **Figure 3-7**. No negative effect on the cell viability of sintered samples are observed as compared to the non-sintered HA control after 24h. To further analyze the extend of cytotoxicity of BT incorporation, the MC3T3-E1 cells were cultured with highly concentrated conditioned media (7days). However, all the samples displayed good cell viability regardless of wt.% of BT incorporation.

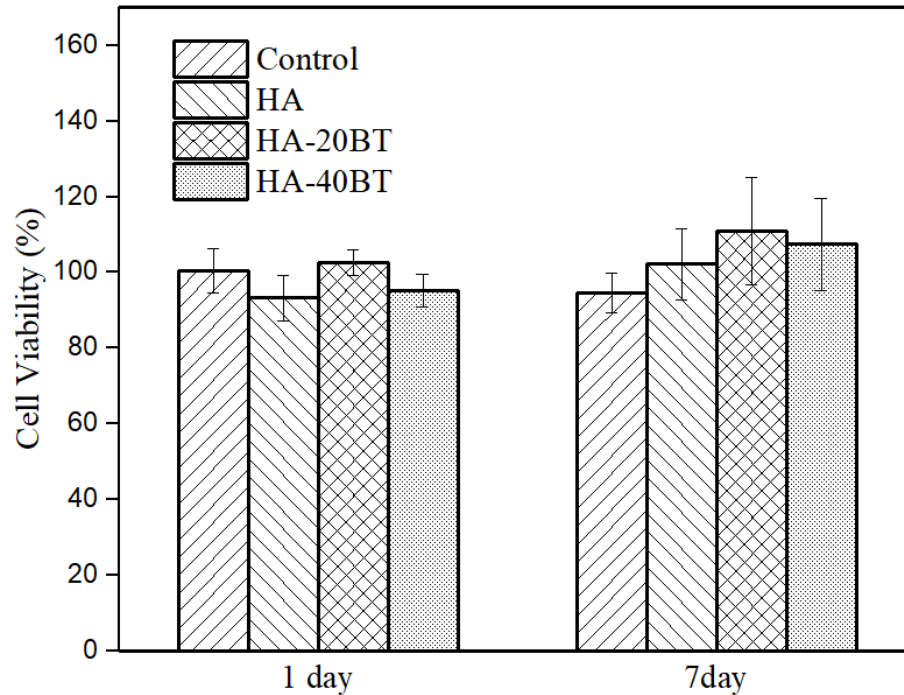


Figure 3-7: Cytocompatibility of HA-x BT sintered samples after 1 and 7 days

3.4 Discussion

The apparent porosity (Table 3.2) of piezobiocomposite HA-xBT sintered samples increased from 10.46 to 25.26% with the addition in BT wt.%. This implies the significant influence of BT on the sintering kinetics and densification of HA-xBT samples. The higher porosity of HA-20/40BT samples accounts for the lower values of hardness and fracture toughness as compared to monolithic HA samples. The preparation of grey body with a low pre-pressing is believed to be the major source of porosity. Dubey et al. (2013) employed SPS technique to prepare HA-BT piezobiocomposites and reported compressive strength of HA-40BT to be 138.3 MPa [43]. Later in 2016, Dubey et al. developed porous nanophase HA-BT composite with porosity of approximately 30% and compressive strength of 236 MPa for 25 vol.% BT [14]. In comparison, in our present study,

conventional sintered HA-20/40BT piezocomposites with a porosity of 22-25%, maintained compressive strength within the range of dentine (295 MPa) and enamel (384 MPa) [34].

The XRD analysis (Figure 3-3) of as-prepared HA sintered samples mainly consists of diffraction peaks of HA and few corresponding to β -TCP. However, with the addition of BT into the sample composition, more dissociation of HA occurs. Furthermore, the reactive sintering occurred such that the reaction between HA and BT generated different phases namely α -TCP, β -TCP, CT, $\text{Ba}_3(\text{PO}_4)_2$ and Ba_2TiO_4 . Prakasam et al. claimed optimum sintering temperature increases with increase in BT content in HA-BT composites which in turn causes the decomposition of HA into β -TCP, α -TCP, CT, $\text{Ba}_{10}(\text{PO}_4)_6(\text{OH})_2$ and loss of OH^- in HA [43,83]. Small amount of β -TCP in HA implant accelerates its bonding with natural bone [38]. Moreover, the formation of anhydrous TCP during sintering enhances in vitro dissolution rate [105]. Thus, with the modulation of sintering parameters and amount of TCP within the HA-xBT samples, we can achieve the coherent bone formation and degradation rate. CT improves the strength, fracture toughness, dielectric properties, conductivity, cell proliferation and differentiation when incorporated within bulk HA sintered biocomposites [40,41,108,109]. Mallik et al. [42] reported 140% increase in osteogenesis at early stage of neobone formation when HA-80wt.% CT were implanted in rabbit femoral bone defects as compared to monolithic HA. Therefore, the presence of CT in our final sintered samples are expected to be beneficial enhancing the cellular activities, growth and differentiation.

The effect of BT addition can also be seen on grain size of as-prepared samples. During the conventional sintering of HA, negligible densification occurs below 900°C, followed

by major densification up to 1150°C, the blowholes start to appear at 1150-1200 °C, and above 1200°C blowholes increase in size and number [105]. Thus, the pores on the surfaces of samples (Figure 3-5(a, c, e)) correspond to blowholes created during exudation of gas. Moreover, the SEM micrograph of as-prepared HA-20/40BT samples (Figure 3-5(c-f)) exhibited wider range of grain size distribution as they possessed coarser grain of 2-3.2 μm (HA-20BT), 2-4.5μm(HA-40BT) and finer grains of 1-2μm. Dubey et al. (2013) reported the bimodal distribution of grain sizes by for conventionally sintered HA-40CT composite [41]. However, in our present study, BT infused samples resulted higher number of finer grains along with normal distribution of grain sizes.

The preliminary assessment of *in vitro* cytocompatibility and bioactivity are most for bioceramics as they guide us whether to move forward with *in vivo* experiments or not. Negative poling of BT and HA-BT sample surfaces assists in the higher cell proliferation and growth than positively charged and uncharged sample surfaces [13,30]. On contrary, Baxter et al. [110] reported insignificant differences regarding *in vitro* cell adhesion, proliferation and viability on poled and unpoled 90% BT samples after 7 days. In our present work, we observed the uniform distribution of apatite layer on the sample surface after 7 days immersion in 1.5× SBF. This proves good *in vitro* bioactivity of as-prepared piezobiocomposites without poling. Furthermore, the cell viability assay provided a strong indication regarding the feasibility of HA-xBT biocomposite as all sintered samples showed no negative effects on viability of MC3T3 cells even at the higher concentration of media corroborating the non-toxic nature of BT and/or CT. Although the results were not significant, HA-20BT showed slightly higher cell viability than other composition

including non-sintered HA control, indicating HA-20BT composition to be an optimum BT wt.% in HA samples when conventional sintering is incorporated.

3.5 Conclusion

The results from present study demonstrated the feasibility of conventional sintering of HA-x BT piezobiocomposites. On contrary to the high-tech and expensive spark plasma sintering technique, the conventional sintering is economical and simpler to operate. In addition, the present work showed higher compressive strength and comparable fracture toughness. The dissociation of HA and BT into various phases such as TCP, CT are expected to be advantages as they may favor the bioactivity, cell responses and dissolution rate of as-prepared composites. Keeping physical, mechanical and biological aspects, the conventional sintered HA-BT samples can be a viable alternative for the load bearing orthopedic applications and demands for the further detailed studies.

Chapter 4

4. Future Works

The development of the smart CPC being a new topic, several studies can be carried out in future for the improvement of mechanical, electrical and biological properties. Aqueous PVA as a liquid phase can improve mechanical properties, setting time and biodegradation. Thus, studies can be carried out on smart CPC with aqueous PVA and/or (colloidal silica + PVA) as the liquid phase. Regarding the electrical properties, a detailed study on the dielectric and piezoelectric values of smart CPC cement should be carried out. Furthermore, the smartness of CPC-BT can be raised to next level if we can synthesize the drug-loaded and gene-loaded smart CPC-BT.

In case of sintered samples, since present study showed the positive responses in terms of *in vitro* bioactivity and cytocompatibility, we aim to study the effects of electrical poling on our samples in future. In addition, considering the dielectric constant of HA-BT samples, we can investigate the feasibility of microwave sintering for the fabrication of such dense piezobiocomposites.

References

1. LeGeros, R. Z. (1988). Calcium phosphate materials in restorative dentistry: a review. *Advances in dental research*, 2(1), 164-180.
2. Koju, N., Sikder, P., Ren, Y., Zhou, H., & Bhaduri, S. B. (2017). Biomimetic coating technology for orthopedic implants. *Current Opinion in Chemical Engineering*, 15, 49-55.
3. Champion, E. (2013). Sintering of calcium phosphate bioceramics. *Acta biomaterialia*, 9(4), 5855-5875.
4. Dorozhkin S. Calcium orthophosphate cements for biomedical application. *J Mater Sci* 2008; 43:3028–3057.
5. Dorozhkin, S. V. (2013). Self-setting calcium orthophosphate formulations. *Journal of functional biomaterials*, 4(4), 209-311.
6. Fukada, E., & Yasuda, I. (1957). On the piezoelectric effect of bone. *Journal of the physical society of Japan*, 12(10), 1158-1162.
7. Fukada, E., & Yasuda, I. (1964). Piezoelectric effects in collagen. *Japanese Journal of Applied Physics*, 3(2), 117.
8. Shamos, M. H., & Lavine, L. S. (1967). Piezoelectricity as a fundamental property of biological tissues. *Nature*, 213(5073), 267-269.
9. Anderson, J. C., & Eriksson, C. (1970). Piezoelectric properties of dry and wet bone. *Nature*, 227(5257), 491-492.

10. Bassett, C. A. L., & Becker, R. O. (1962). Generation of electric potentials by bone in response to mechanical stress. *Science*, 137(3535), 1063-1064.
11. Bassett, C. A. L. (1965). Electrical effects in bone. *Scientific American*, 213(4), 18-25.
12. Platt, S. R., Farritor, S., Garvin, K., & Haider, H. (2005). The use of piezoelectric ceramics for electric power generation within orthopedic implants. *IEEE/ASME Transactions on Mechatronics*, 10(4), 455-461.
13. Dubey, A. K., & Basu, B. (2014). Pulsed Electrical Stimulation and Surface Charge Induced Cell Growth on Multistage Spark Plasma Sintered Hydroxyapatite-Barium Titanate Piezobiocomposite. *Journal of the American Ceramic Society*, 97(2), 481-489.
14. Dubey, A. K., & Kakimoto, K. I. (2016). Impedance spectroscopy and mechanical response of porous nanophase hydroxyapatite–barium titanate composite. *Materials Science and Engineering: C*, 63, 211-221.
15. Fredericks, D. C., Smucker, J., Petersen, E. B., Bobst, J. A., Gan, J. C., Simon, B. J., & Glazer, P. (2007). Effects of direct current electrical stimulation on gene expression of osteopromotive factors in a posterolateral spinal fusion model. *Spine*, 32(2), 174-181.
16. Park, J. B., & Kenner, G. H. (1975). Effect of Electrical Stimulation on the Tensile Strength of the Porous Implant and Bone Interfac. *Biomaterials, medical devices, and artificial organs*, 3(2), 233-243.
17. Park, J. B., & Kenner, G. H. (1976). Effect of electrical stimulation on the interfacial tensile strength and amount of bone formation. *Biomaterials, medical devices, and artificial organs*, 4(2), 225-233.

18. Park, J. B., Young, S. O., Kenner, G. H., Von Recum, A. F., Myers, B. R., & Moore, R. R. (1978). Dental Implant Fixation by Electrically Mediated Process II. Tissue Ingrowth. *Biomaterials, medical devices, and artificial organs*, 6(4), 291-303.
19. Park, Y. S. O., Kenner, J. B., Moore, G. H., Myers, R. R., & Sauer, B. R. (1978). Dental Implant Fixation by Electrically Mediated Process I. Interfacial Strength. *Biomaterials, medical devices, and artificial organs*, 6(2), 111-126.
20. Tobaben, E. J., Goetzinger, N. C., Domann, J. P., Barrett-Gonzalez, R., Arnold, P. M., & Friis, E. A. (2014). Stacked macro fiber piezoelectric composite generator for a spinal fusion implant. *Smart Materials and Structures*, 24(1), 017002
21. Jianqing, F., Huipin, Y., & Xingdong, Z. (1997). Promotion of osteogenesis by a piezoelectric biological ceramic. *Biomaterials*, 18(23), 1531-1534.
22. Williams, W. S., & Breger, L. (1975). Piezoelectricity in tendon and bone. *Journal of biomechanics*, 8(6), 407-413.
23. Arlt, G., Hennings, D., & De With, G. (1985). Dielectric properties of fine-grained barium titanate ceramics. *Journal of applied physics*, 58(4), 1619-1625.
24. Wang, J. J., Meng, F. Y., Ma, X. Q., Xu, M. X., & Chen, L. Q. (2010). Lattice, elastic, polarization, and electrostrictive properties of BaTiO₃ from first-principles. *Journal of Applied Physics*, 108(3), 034107.
25. Park, J. B., Von Recum, A. F., Kenner, G. H., Kelly, B. J., Coffeen, W. W., & Grether, M. F. (1980). Piezoelectric ceramic implants: a feasibility study. *Journal of Biomedical Materials Research Part A*, 14(3), 269-277.

26. Grether, M. F., Coffeen, W. W., Kenner, G. H., & Park, J. B. (1980). The mechanical stability of barium titanate (ceramic) implants in Vitro. *Biomaterials, medical devices, and artificial organs*, 8(3), 265-272.
27. Park, J. B., Kelly, B. J., Kenner, G. H., Von Recum, A. F., Grether, M. F., & Coffeen, W. W. (1981). Piezoelectric ceramic implants: in vivo results. *Journal of Biomedical Materials Research Part A*, 15(1), 103-110.
28. Beloti, M. M., de Oliveira, P. T., Gimenes, R., Zaghete, M. A., Bertolini, M. J., & Rosa, A. L. (2006). In vitro biocompatibility of a novel membrane of the composite poly (vinylidene-trifluoroethylene)/barium titanate. *Journal of biomedical materials research Part A*, 79(2), 282-288.
29. Dubey, A. K., Thirvikraman, G., & Basu, B. (2015). Absence of systemic toxicity in mouse model towards BaTiO₃ nanoparticulate based eluate treatment. *Journal of Materials Science: Materials in Medicine*, 26(2), 1-11.
30. Park, Y. J., Hwang, K. S., Song, J. E., Ong, J. L., & Rawls, H. R. (2002). Growth of calcium phosphate on poling treated ferroelectric BaTiO₃ ceramics. *Biomaterials*, 23(18), 3859-3864.
31. Brown, P. W. (1992). Phase Relationships in the Ternary System CaO—P₂O₅—H₂O at 25° C. *Journal of the American Ceramic Society*, 75(1), 17-22.
32. German, R. (2014). *Sintering: from empirical observations to scientific principles*. Butterworth-Heinemann.
33. Bellucci, D., Desogus, L., Montinaro, S., Orrù, R., Cao, G., & Cannillo, V. (2017). Innovative hydroxyapatite/bioactive glass composites processed by spark plasma

- sintering for bone tissue repair. *Journal of the European Ceramic Society*, 37(4), 1723-1733.
34. Akao, M., Aoki, H., & Kato, K. (1981). Mechanical properties of sintered hydroxyapatite for prosthetic applications. *Journal of Materials Science*, 16(3), 809-812.
35. Karimzadeh, A., Ayatollahi, M. R., Bushroa, A. R., & Herliansyah, M. K. (2014). Effect of sintering temperature on mechanical and tribological properties of hydroxyapatite measured by nanoindentation and nanoscratch experiments. *ceramics international*, 40(7), 9159-9164.
36. Heidari, F., Razavi, M., Ghaedi, M., Forooghi, M., Tahriri, M., & Tayebi, L. (2017). Investigation of mechanical properties of natural hydroxyapatite samples prepared by cold isostatic pressing method. *Journal of Alloys and Compounds*, 693, 1150-1156.
37. Cuccu, A., Montinaro, S., Orrù, R., Cao, G., Bellucci, D., Sola, A., & Cannillo, V. (2015). Consolidation of different hydroxyapatite powders by SPS: Optimization of the sintering conditions and characterization of the obtained bulk products. *Ceramics International*, 41(1), 725-736.
38. Monmaturapoj, N., & Yatonchai, C. (2017). Effect of sintering on microstructure and properties of hydroxyapatite produced by different synthesizing methods. *Journal of Metals, Materials and Minerals*, 20(2).
39. Maidaniuc, A., Miculescu, F., MOCANU, A. C., VOICU, Ș. I., Miculescu, M., Purcaru, A., ... & Rada, M. E. (2017). SINTERABILITY STUDY OF BOVINE-DERIVED HYDROXYAPATITE AND SILVER MICROCOMPOSITES. *UNIVERSITY POLITEHNICA OF BUCHAREST SCIENTIFIC BULLETIN*

- SERIES C-ELECTRICAL ENGINEERING AND COMPUTER SCIENCE, 79(1), 145-154.
40. Ravikumar, K., Mallik, P. K., & Basu, B. (2016). Twinning induced enhancement of fracture toughness in ultrafine grained Hydroxyapatite–Calcium Titanate composites. *Journal of the European Ceramic Society*, 36(3), 805-815.
41. Dubey, A. K., Mallik, P. K., Kundu, S., & Basu, B. (2013). Dielectric and electrical conductivity properties of multi-stage spark plasma sintered HA–CaTiO₃ composites and comparison with conventionally sintered materials. *Journal of the European Ceramic Society*, 33(15), 3445-3453.
42. Mallik, P. K., & Basu, B. (2014). Better early osteogenesis of electroconductive hydroxyapatite–calcium titanate composites in a rabbit animal model. *Journal of Biomedical Materials Research Part A*, 102(3), 842-851.
43. Dubey, A. K., EA, A., Balani, K., & Basu, B. (2013). Multifunctional Properties of Multistage Spark Plasma Sintered HA–BaTiO₃-Based Piezobiocomposites for Bone Replacement Applications. *Journal of the American Ceramic Society*, 96(12), 3753-3759.
44. Zhou, H., Agarwal, A. K., Goel, V. K., & Bhaduri, S. B. (2013). Microwave assisted preparation of magnesium phosphate cement (MPC) for orthopedic applications: a novel solution to the exothermicity problem. *Materials Science and Engineering: C*, 33(7), 4288-4294.
45. Lewis, G. (2006). Injectable bone cements for use in vertebroplasty and kyphoplasty: State-of-the-art review. *Journal of Biomedical Materials Research Part B: Applied Biomaterials*, 76(2), 456-468.

46. Dadkhah, M., Pontiroli, L., Fiorilli, S., Manca, A., Tallia, F., Tcacencu, I., & Vitale-Brovarone, C. (2017). Preparation and characterisation of an innovative injectable calcium sulphate based bone cement for vertebroplasty application. *Journal of Materials Chemistry B*, 5(1), 102-115.
47. Bohner, M., Gbureck, U., & Barralet, J. E. (2005). Technological issues for the development of more efficient calcium phosphate bone cements: a critical assessment. *Biomaterials*, 26(33), 6423-6429.
48. Tas, A. C., & Aldinger, F. (2005). Formation of apatitic calcium phosphates in a Na-K-phosphate solution of pH 7.4. *Journal of Materials Science: Materials in Medicine*, 16(2), 167-174.
49. Constantz, B. R., Ison, I. C., Fulmer, M. T., Poser, R. D., Smith, S. T., VanWagoner, M., ... & Rosenthal, D. I. (1995). Skeletal repair by in situ formation of the mineral phase of bone. *Science*, 267(5205), 1796-1799.
50. Mirtchi, A. A., Lemaitre, J., & Terao, N. (1989). Calcium phosphate cements: Study of the β -tricalcium phosphate—monocalcium phosphate system. *Biomaterials*, 10(7), 475-480.
51. Tamimi, F., Sheikh, Z., & Barralet, J. (2012). Dicalcium phosphate cements: Brushite and monetite. *Acta biomaterialia*, 8(2), 474-487.
52. Bohner, M. (2000). Calcium orthophosphates in medicine: from ceramics to calcium phosphate cements. *Injury*, 31, D37-D47.
53. Bohner, M. (2001). Physical and chemical aspects of calcium phosphates used in spinal surgery. *European Spine Journal*, 10(2), S114-S121.

54. Desai, T. R., Bhaduri, S. B., & Tas, A. C. (2007). A self-setting, monetite (CaHPO₄) cement for skeletal repair. *Adv. Bioceram. Biocompos. II*, 27, 61-69.
55. Tas, A. C. (2009). Monetite (CaHPO₄) synthesis in ethanol at room temperature. *Journal of the American Ceramic Society*, 92(12), 2907-2912.
56. Cama, G., Gharibi, B., Sait, M. S., Knowles, J. C., Lagazzo, A., Romeed, S., ... & Deb, S. (2013). A novel method of forming micro-and macroporous monetite cements. *Journal of Materials Chemistry B*, 1(7), 958-969.
57. Tamimi, F., Torres, J., Bassett, D., Barralet, J., & Cabarcos, E. L. (2010). Resorption of monetite granules in alveolar bone defects in human patients. *Biomaterials*, 31(10), 2762-2769.
58. Tamimi, F., Le Nihouannen, D., Eimar, H., Sheikh, Z., Komarova, S., & Barralet, J. (2012). The effect of autoclaving on the physical and biological properties of dicalcium phosphate dihydrate bioceramics: brushite vs. monetite. *Acta biomaterialia*, 8(8), 3161-3169.
59. Tamimi, F., Torres, J., Kathan, C., Baca, R., Clemente, C., Blanco, L., & Cabarcos, E. L. (2008). Bone regeneration in rabbit calvaria with novel monetite granules. *Journal of biomedical materials research Part A*, 87(4), 980-985.
60. Tamimi, F., Torres, J., Gbureck, U., Lopez-Cabarcos, E., Bassett, D. C., Alkhraisat, M. H., & Barralet, J. E. (2009). Craniofacial vertical bone augmentation: a comparison between 3D printed monolithic monetite blocks and autologous onlay grafts in the rabbit. *Biomaterials*, 30(31), 6318-6326.

61. Montazerolghaem, M., Ott, M. K., Engqvist, H., Melhus, H., & Rasmusson, A. J. (2015). Resorption of monetite calcium phosphate cement by mouse bone marrow derived osteoclasts. *Materials Science and Engineering: C*, 52, 212-218.
62. Stulajterova, R., Medvecky, L., Giretova, M., & Sopcak, T. (2015). Structural and phase characterization of bioceramics prepared from tetracalcium phosphate–monetite cement and in vitro osteoblast response. *Journal of Materials Science: Materials in Medicine*, 26(5), 183.
63. Sheikh, Z., Zhang, Y. L., Grover, L., Merle, G. E., Tamimi, F., & Barralet, J. (2015). In vitro degradation and in vivo resorption of dicalcium phosphate cement based grafts. *Acta biomaterialia*, 26, 338-346.
64. Touny, A. H., Dawkins, H., Zhou, H., & Bhaduri, S. B. (2011). Hydrolysis of monetite/chitosan composites in α -MEM and SBF solutions. *Journal of Materials Science: Materials in Medicine*, 22(5), 1101-1109.
65. Touny, A. H., & Bhaduri, S. B. (2010). A reactive electrospinning approach for nanoporous PLA/monetite nanocomposite fibers. *Materials Science and Engineering: C*, 30(8), 1304-1312.
66. Boroujeni N. M., Zhou H., Luchini Timothy J. F., Bhaduri S. B. 2014. Development of monetite/phosphorylated chitosan composite bone cement. *J Biomed Mater Res Part B* 2014;102B:260–266.
67. Boroujeni, N. M., Zhou, H., Luchini, T. J., & Bhaduri, S. B. (2013). Development of multi-walled carbon nanotubes reinforced monetite bionanocomposite cements for orthopedic applications. *Materials Science and Engineering: C*, 33(7), 4323-4330.

68. Zhou, H., Luchini, T. J., Agarwal, A. K., Goel, V. K., & Bhaduri, S. B. (2014). Development of monetite–nanosilica bone cement: A preliminary study. *Journal of Biomedical Materials Research Part B: Applied Biomaterials*, 102(8), 1620-1626.
69. Zhou, H., Luchini, T. J., Boroujeni, N. M., Agarwal, A. K., Goel, V. K., & Bhaduri, S. B. (2015). Development of nanosilica bonded monetite cement from egg shells. *Materials Science and Engineering: C*, 50, 45-51.
70. Carrodeguas, R. G., V´zquez, B., del Barrio, J. S. R., & de la Cal, A. M. (2002). Barium titanate-filled bone cements. I. Chemical, physical, and mechanical characterization. *International Journal of Polymeric Materials*, 51(7), 591-605.
71. Bohner, M., Galea, L., & Doebelin, N. (2012). Calcium phosphate bone graft substitutes: Failures and hopes. *Journal of the european ceramic society*, 32(11), 2663-2671.
72. Schmitz, J. P., Hollinger, J. O., & Milam, S. B. (1999). Reconstruction of bone using calcium phosphate bone cements: a critical review. *Journal of Oral and Maxillofacial Surgery*, 57(9), 1122-1126.
73. Constantz, B. R., Barr, B. M., Ison, I. C., Fulmer, M. T., Baker, J., McKinney, L., ... & Poser, R. D. (1998). Histological, chemical, and crystallographic analysis of four calcium phosphate cements in different rabbit osseous sites. *Journal of Biomedical Materials Research Part A*, 43(4), 451-461.
74. Klammert U, Reuther T, Jahn C, Kraski B, K€ubler AC, Gbureck U. Cytocompatibility of brushite and monetite cell culture scaffolds made by three-dimensional powder printing. *Acta Biomater* 2009; 5:727-734.

75. Bassett, C. A. L. (1967). Biologic significance of piezoelectricity. *Calcified Tissue International*, 1(1), 252-272.
76. Marino, A. A., & Becker, R. O. (1970). Piezoelectric effect and growth control in bone. *Nature*, 228(5270), 473-474.
77. Marino, A. A., Becker, R. O., & Soderholm, S. C. (1971). Origin of the piezoelectric effect in bone. *Calcified Tissue International*, 8(1), 177-180.
78. Williams, W. S., & Breger, L. (1975). Piezoelectricity in tendon and bone. *Journal of biomechanics*, 8(6), 407-413.
79. Reddy, G. N., & Saha, S. (1984). Electrical and dielectric properties of wet bone as a function of frequency. *IEEE transactions on biomedical engineering*, (3), 296-303.
80. El Messierey, M. A., Hastings, G. W., & Rakowski, S. (1979). Ferro-electricity of dry cortical bone. *Journal of biomedical engineering*, 1(1), 63-65.
81. Lang, S. B. (1966). Pyroelectric effect in bone and tendon. *Nature*, 212(5063), 704-705.
82. Kosterich, J. D., Foster, K. R., & Pollack, S. R. (1983). Dielectric permittivity and electrical conductivity of fluid saturated bone. *IEEE Transactions on Biomedical Engineering*, (2), 81-86.
83. Prakasam, M., Albino, M., Lebraud, E., Maglione, M., Elissalde, C., & Largeteau, A. (2017). Hydroxyapatite-barium titanate piezocomposites with enhanced electrical properties. *Journal of the American Ceramic Society*, 100(6), 2621-2631.
84. Genchi, G. G., Marino, A., Rocca, A., Mattoli, V., & Ciofani, G. (2016). Barium titanate nanoparticles: promising multitasking vectors in nanomedicine. *Nanotechnology*, 27(23), 232001.

85. Carrodeguas, R. G., Lasa, B. V., & Del Barrio, J. S. R. (2004). Injectable acrylic bone cements for vertebroplasty with improved properties. *Journal of Biomedical Materials Research Part B: Applied Biomaterials*, 68(1), 94-104.
86. Jalota S, Bhaduri SB, Tas AC. Effect of carbonate content and buffer type on calcium phosphonate formation in SBF solutions. *J Mater Sci Mater Med*. 2006; 17:697–707.
87. Åberg, J., Pankotai, E., Hulsart Billström, G., Weszl, M., Larsson, S., Forster-Horváth, C., ... & Engqvist, H. (2011). In vivo evaluation of an injectable premixed radiopaque calcium phosphate cement. *International journal of biomaterials*, 2011.
88. Takagi, S., Chow, L. C., Hirayama, S., & Eichmiller, F. C. (2003). Properties of elastomeric calcium phosphate cement–chitosan composites. *Dental materials*, 19(8), 797-804.
89. Wu F, Su J, Wei J, Guo H and Liu C 2008 Injectable bioactive calcium–magnesium phosphate cement for bone regeneration *Biomed. Mater.* 3 044105.
90. Wu F, Wei J, Guo H, Chen F, Hong H and Liu C 2008 Selfsetting bioactive calcium–magnesium phosphate cement with high strength and degradability for bone regeneration *Acta Biomater.* 4 1873–84.
91. Babaie, E., Lin, B., Goel, V. K., & Bhaduri, S. B. (2016). Evaluation of amorphous magnesium phosphate (AMP) based non-exothermic orthopedic cements. *Biomedical Materials*, 11(5), 055010.
92. Ren F, Ding Y, Leng Y. 2014. Infrared spectroscopic characterization of carbonated apatite: A combined experimental and computational study. *J Biomed Mater Res Part A* 2014:102A:496–505.

93. Borhan, S., Hesaraki, S., & Ahmadzadeh-Asl, S. (2010). Evaluation of colloidal silica suspension as efficient additive for improving physicochemical and in vitro biological properties of calcium sulfate-based nanocomposite bone cement. *Journal of Materials Science: Materials in Medicine*, 21(12), 3171-3181.
94. Ding, S., Zhang, J., Tian, Y., Huang, B., Yuan, Y., & Liu, C. (2016). Magnesium modification up-regulates the bioactivity of bone morphogenetic protein-2 upon calcium phosphate cement via enhanced BMP receptor recognition and Smad signaling pathway. *Colloids and Surfaces B: Biointerfaces*, 145, 140-151.
95. Salimi, M. H., Heughebaert, J. C., & Nancollas, G. H. (1985). Crystal growth of calcium phosphates in the presence of magnesium ions. *Langmuir*, 1(1), 119-122.
96. Rude, R. K., Gruber, H. E., Wei, L. Y., Frausto, A., & Mills, B. G. (2003). Magnesium deficiency: effect on bone and mineral metabolism in the mouse. *Calcified tissue international*, 72(1), 32-41.
97. Mestres, G., & Ginebra, M. P. (2011). Novel magnesium phosphate cements with high early strength and antibacterial properties. *Acta biomaterialia*, 7(4), 1853-1861.
98. Ohgaki, M., Kizuki, T., Katsura, M., & Yamashita, K. (2001). Manipulation of selective cell adhesion and growth by surface charges of electrically polarized hydroxyapatite. *Journal of Biomedical Materials Research Part A*, 57(3), 366-373.
99. Hesaraki, S., Alizadeh, M., Borhan, S., & Pourbaghi-Masouleh, M. (2012). Polymerizable nanoparticulate silica-reinforced calcium phosphate bone cement. *Journal of Biomedical Materials Research Part B: Applied Biomaterials*, 100(6), 1627-1635.

100. Simon, J., & Simon, B. (2008). Electrical bone stimulation. In *Musculoskeletal Tissue Regeneration* (pp. 259-287). Humana Press.
101. Nacer, R. S., Silva, B. A. K. D., Poppi, R. R., Silva, D. K. M., Cardoso, V. S., Delben, J. R. J., & Delben, A. A. S. T. (2015). Biocompatibility and osteogenesis of the castor bean polymer doped with silica (SiO₂) or barium titanate (BaTiO₃) nanoparticles. *Acta cirurgica brasileira*, 30(4), 255-263.
102. Ciofani, G., Ricotti, L., Canale, C., D'Alessandro, D., Berrettini, S., Mazzolai, B., & Mattoli, V. (2013). Effects of barium titanate nanoparticles on proliferation and differentiation of rat mesenchymal stem cells. *Colloids and Surfaces B: Biointerfaces*, 102, 312-320.
103. Ciofani, G., Danti, S., D'Alessandro, D., Moscato, S., Petrini, M., & Menciassi, A. (2010). Barium titanate nanoparticles: highly cytocompatible dispersions in glycol-chitosan and doxorubicin complexes for cancer therapy. *Nanoscale research letters*, 5(7), 1093.
104. Ball, J. P., Mound, B. A., Nino, J. C., & Allen, J. B. (2014). Biocompatible evaluation of barium titanate foamed ceramic structures for orthopedic applications. *Journal of Biomedical Materials Research Part A*, 102(7), 2089-2095.
105. Ruys, A. J., Wei, M., Sorrell, C. C., Dickson, M. R., Brandwood, A., & Milthorpe, B. K. (1995). Sintering effects on the strength of hydroxyapatite. *Biomaterials*, 16(5), 409-415.
106. Spiegler, R., Schmauder, S., & Sigl, L. S. (1990). Fracture toughness evaluation of WC-Co alloys by indentation testing. *Journal of Hard Materials*, 1(3), 147-158.

107. Rehman, I., & Bonfield, W. (1997). Characterization of hydroxyapatite and carbonated apatite by photo acoustic FTIR spectroscopy. *Journal of Materials Science: Materials in Medicine*, 8(1), 1-4.
108. Thirvikraman, G., Mallik, P. K., & Basu, B. (2013). Substrate conductivity dependent modulation of cell proliferation and differentiation in vitro. *Biomaterials*, 34(29), 7073-7085.
109. Ozturk, S., & Yetmez, M. (2016). Studies on Characterization of Bovine Hydroxyapatite/CaTiO₃ Biocomposites. *Advances in Materials Science and Engineering*, 2016.
110. Baxter, F. R., Turner, I. G., Bowen, C. R., Gittings, J. P., & Chaudhuri, J. B. (2009). An in vitro study of electrically active hydroxyapatite-barium titanate ceramics using Saos-2 cells. *Journal of Materials Science: Materials in Medicine*, 20(8), 1697-1708.